A NUMERICAL STUDY OF THE VALIDITY OF SHALLOW ICE APPROXIMATIONS

Josefin Ahlkrona[1], Nina Kirchner[2,3], and Per Lötstedt[1]

[1] *Uppsala University, Division of Scientific Computing, Department of Information Technology, Uppsala, Sweden*
[2] *Stockholm University, Department of Physical Geography and Quaternary Geology, Stockholm, Sweden*
[3] *Stockholm University, Bert Bolin Center for Climate Research, Stockholm, Sweden*

Abstract

Improving numerical ice sheet models is a very active field of research. In part, this is because ice sheet modelling has gained societal relevance in the context of predictions of future sea level rise. Ice sheet modelling is however also a challenging mathematical and computational subject. Since the exact equations governing ice dynamics, the full Stokes equations, are computationally expensive to solve, approximations are crucially needed for many problems. Shallow ice approximations are a family of approximations derived by asymptotic expansion of the exact equations in terms of the aspect ratio, ϵ. Retaining only the zeroth order terms in this expansion yields the by far most frequently used approximation; the Shallow Ice Approximation (SIA). Including terms up to second order yields the Second Order Shallow Ice Approximation (SOSIA), which is a so-called higher order model. Here, we study the validity and accuracy of shallow ice approximations beyond previous analyses of the SIA. We perform a detailed analysis of the assumptions behind shallow ice approximations, i.e. of the order of magnitude of field variables. We do this by using a numerical solution of the exact equations for ice flow over a sloping, undulating bed. We also construct analytical solutions for the SIA and SOSIA and numerically compute the accuracy for varying ϵ by comparing to the exact solution. We find that the assumptions underlying shallow ice approximations are not entirely appropriate since they do not account for a high viscosity boundary layer developing near the ice surface as soon as small bumps are introduced at the ice base. This boundary layer is thick and has no distinct border. Other existing theories which do incorporate the boundary layer are in better, but not full, agreement with our numerical results. Our results reveal that neither the SIA nor the SOSIA is as accurate as suggested by the asymptotic expansion approach. Also, in SOSIA the ice rheology needs to be altered to avoid infinite viscosity, though both our analytical and numerical solutions show that, especially for high bump amplitudes, the accuracy of the SOSIA is highly sensitive to this alternation. However, by updating the SOSIA solution in an iterative manner, we obtain a model which utilises the advantages of shallow ice approximations, while reducing the disadvantages.

1. Introduction

Ice sheets and glaciers are important components of the global climate system, and both theoretical analysis and numerical modelling are important tools for understanding ice dynamics. For a review of ice sheets, glaciers, and ice sheet modelling, cf. (**1**, **2**, **3**). Ice dynamics is governed by the so-called full Stokes equations. These are computationally expensive to solve, in particular since ice is a non-Newtonian fluid. Until recently, grounded ice sheets were mainly modelled by the Shallow Ice Approximation (SIA). The SIA is a crude approximation for grounded ice sheets that is computationally cheap. It is accurate in the interior of an ice sheet, but not at the margins where ice dynamics is more complicated due to ice streaming and coupling to ice shelves. As both computer power and interest in marginal ice dynamics have grown, higher order approximations (i.e. approximations that are more accurate than SIA) and full Stokes models have developed. However, for several interesting problems, such as paleoglacial systems, the full Stokes models and most existing higher order models are still too expensive to use. Therefore the need for approximations like the SIA and fast higher order models remains.

The SIA utilises the fact that ice sheets are shallow, and was derived independently by Hutter (**4**) and Morland (**5**) in the beginning of the 1980's. The derivation is based on scaling the full Stokes equations, and expanding them in power series in terms of the *aspect ratio*, ϵ, which is a small parameter measuring the shallowness of an ice sheet. The SIA is the lowest (zeroth) order approximation in this expansion. In the end of the 1990's, the Second Order Shallow Ice Approximation (SOSIA) was derived by Baral et al. (**6**, **7**), pushing the series expansion to second order in ϵ. The SOSIA is thus a higher order model based on a formal expansion in ϵ, which is almost as computationally cheap as the SIA. The SOSIA equations, as described in (**6**), have however never been put into practical use.

When scaling the full Stokes equations in order to derive shallow ice approximations (meaning both SIA and SOSIA), assumptions on how variables such as stresses and velocities vary with the aspect ratio are required. The scaling assumptions in (**6**, **7**, **8**) are thus the foundation of shallow ice approximations and the basis for much theoretical analysis of ice dynamics. However, other scalings have been applied in both analysis and model development. For example, one of the most popular higher order models, the Blatter-Pattyn equations (**9**, **10**), is based on a different scaling by Blatter (**9**). This scaling is not consistent in itself, but the model has recently been justified by Schoof & Hindmarsh in (**11**).

It has also been discussed whether different scalings should be used in different regions of the ice. Johnson & McMeeking (**12**) suggested that the equations should be rescaled in a boundary layer near the ice surface, where the viscosity is high due to the non-linear, singular rheology of ice, cf. also Schoof & Hindmarsh (**11**). Baral et al. (**6**) dismissed this as too complicated and introduced a parameter, σ_{res}, instead to regularise the rheology near the surface, following earlier suggestions by (**13**, **14**).

Yet, from a practical point of view, the SIA made it possible, for the first time, to simulate continental and hemisphere-scale glaciations during entire glacial cycles (**15**, **16**, **17**, **18**, **19**, **20**, **21**). Along with its success, a few guidelines as to the limitations inherent to the SIA have become widely known. These include that shallow ice approximations are

valid for aspect ratios, ϵ, up to around 10^{-2}, and that shallow ice approximations are more accurate when the bedrock slope is small and bumps are smooth, cf. e.g. (**1**). However, the different, conflicting ways of scaling as well as the relatively broad span of results obtained in a recent ice model inter-comparison, the ISMIP-HOM benchmark (**22**, **23**), have raised our curiosity as to the validity of the *foundations* of different approximation schemes employed in ice sheet modelling. Learning more about the theory behind shallow ice approximations, and thereby about the magnitude of the terms in the full Stokes equations, can also be useful when developing higher order or full Stokes codes with a fast convergence rate.

Therefore, we investigate the validity and accuracy of shallow ice approximations, including both the SIA and the SOSIA. More specifically we address the following questions: How do the velocities, stresses and pressure vary with ϵ in accurate numerical solutions using the full Stokes solver Elmer (**24**, **25**), and how do these scaling relations agree with the assumptions in Baral et al. (**7**, **8**), Blatter (**9**) and Schoof & Hindmarsh (**11**)? Is there a boundary layer close to the ice surface where the field variables scale differently due to the non-linear rheology of ice? Do scaling relations depend on other geometrical quantities than the aspect ratio ϵ, and, if yes, on which and how? Are the SIA and the SOSIA as accurate in numerical simulations (in comparison with Elmer solutions) as the theory in Baral et al. (**6**) asserts? How should the singular rheology of ice be treated in SOSIA? Is the SOSIA a possible tool to tackle paleoglacial simulations?

In order to answer these questions we briefly describe the full Stokes equations, the theory of shallow ice approximations, and different ways of handling the singular rheology of ice, in Section 2. Section 3 introduces our model problem, which is an extension of the ISMIP-HOM B benchmark experiment (**22**, **23**), i.e. ice flow over a bumpy bed with no-slip conditions at the base. In Section 4 we present numerically computed scaling relations for the field variables, obtained by solving the full Stokes equations with the code Elmer (**24**, **25**) for the problem introduced in Section 3 and compare with theory in Baral et al. (**7**, **8**), Blatter (**9**) and Schoof & Hindmarsh (**11**). The SIA has been anlysed before by comparing to full Stokes solutions (**25**, **26**, **27**), but to our knowledge this is the first time the underlying *assumptions* in the derivation of the shallow ice approximation are evaluated by using a full Stokes code. In Section 5.2 an analytical SOSIA solution for the model problem of Section 3 is presented and discussed, extending previous work by Baral et al. (**6**, **7**). In Section 5.4 we implement the SOSIA numerically and experiment with different ways of handling the infinite viscosities. We also compute the accuracy of both the SIA and the SOSIA by comparing with the solution obtained with Elmer, for varying ϵ. The SOSIA is solved iteratively in the end of Section 5.4, followed by a discussion and conclusions in Section 6.

2. Theory

2.1 *Governing Equations*

Isothermal flow of natural ice masses is governed by the balance of mass, balance of linear momentum, and a constitutive law for the (symmetric) Cauchy stress tensor:

$$0 = \operatorname{div} \mathbf{v}, \tag{2.1}$$

$$\rho \dot{\mathbf{v}} = -\nabla p + \operatorname{div} \mathbf{T}^D + \rho \mathbf{g}. \tag{2.2}$$

Here, ρ is the density, $\mathbf{v}$ the velocity field, $\mathbf{T}^D$ the deviatoric stress tensor, $\mathbf{g}$ gravitational acceleration, and $\mathbf{D} := (\mathbf{v} + \mathbf{v}^*)/2$ the strain rate tensor, where * denotes transpose. $\mathbf{T}^D$

is related to the Cauchy stress, $\mathbf{T}$, as $\mathbf{T} = -p\mathbf{I} + \mathbf{T}^D$, where p is the pressure. $\dot{\mathbf{v}}$ denotes the total (material) time derivative of the velocity. The constitutive equation relating stress and strain rate is Glen's flow law,

$$\mathbf{D} \quad = \quad \mathcal{A}(T')f(\sigma)\mathbf{T}^D, \tag{2.3}$$

describing ice as a non-Newtonian fluid with viscosity, η, given by $1/\eta = 2\mathcal{A}(T')f(\sigma)$. $\mathcal{A}(T')$ is the so-called rate factor, accounting for the dependence of the viscosity on the pressure melting point corrected temperature T'. For isothermal conditions $\mathcal{A}$ is a constant. f is the creep response function, defined by $f(\sigma) = \sigma^{n-1}$, where we let $n = 3$. Its argument σ, the effective stress, is the square root of the second invariant of $\mathbf{T}^D$, and is defined by

$$\sigma^2 = \frac{1}{2}\mathrm{tr}\,(\mathbf{T}^D)^2 = (t^D_{xz})^2 + (t^D_{yz})^2 + (t^D_{xy})^2 + \frac{1}{2}\left((t^D_{xx})^2 + (t^D_{yy})^2 + (t^D_{zz})^2\right). \tag{2.4}$$

Here, t^D_{ij} $(i, j = x, y, z)$ are the components of $\mathbf{T}^D$ in a Cartesian coordinate system where the z-axis is pointing in the opposite direction of gravity. We refer to t^D_{xx}, t^D_{yy} and t^D_{zz} as *normal deviatoric stresses*, t^D_{xz} $(= t_{xz})$ and t^D_{yz} $(= t_{yz})$ as *vertical shear stresses* and t^D_{xy} $(= t_{xy})$ as the *horizontal plane shear stress*. In glaciology it is also common to use the term *longitudinal stresses* for t^D_{xx}, t^D_{yy}, t^D_{zz} and t^D_{xy}.

Due to the low Reynolds number of ice, the acceleration term in (2) is very small; neglecting it corresponds to imposing the Stokes approximation. In certain approximation schemes, $\rho\dot{\mathbf{v}} \approx 0$ is derived rather than imposed (see Section 2.2). Employing the Stokes approximation is common to all numerical ice codes; differences arise in the approximations made to the right hand side of (2). If all components of the stress tensor are accounted for, ice modellers typically refer to (2) as the full-Stokes equations.

2.2 *Shallow Ice Approximations*

Shallow ice approximations are used to simplify (1)-(4) and rely on the basic assumption that ice sheets are shallow, i.e. that their horizontal extent is much larger than their vertical one. The ratio between thickness and horizontal extent defines the aspect ratio ϵ, which is of the order 10^{-3} for large ice sheets and 10^{-1} for glaciers (**1**). The aspect ratio is used as a perturbation parameter: all variables are scaled to dimensionless form in terms of ϵ and then expanded into power series. A hierarchy of models can then be derived ('zero order', 'first order', 'second order' etc.), characterised by the powers of ϵ that are retained (**2**, **4**, **5**, **6**).

2.2.1 Scaling

Scalings proposed in the literature can be described as either 1) uniform, by which we mean that a single scaling is proposed for the bulk of an ice sheet (**4**, **5**, **7**, **8**, **9**), or 2) non-uniform, refering to that different scalings are proposed for different regions of an ice sheet, resolving, e.g. boundary layers (**11**, **12**). These non-uniform scalings may extend the applicability of the SIA beyond the limits set by uniform scalings. In the following we present the uniform scaling used in (**6**, **8**) and show how shallow ice approximations are derived from it. In Section 4 we also present an alternative uniform scaling (proposed by Blatter (**9**)), as well

as a non-uniform scaling, i.e. the one by Schoof & Hindmarsh (**11**) in order to compare with numerically computed scaling relations.

For brevity, the scaling (and power series expansion, see Section 2.2.2) is exemplified for the momentum balance (2) , which, in component form, is

$$\begin{aligned}
\rho\dot{v}_x &= -\frac{\partial p}{\partial x} + \frac{\partial {t^D}_{xx}}{\partial x} + \frac{\partial {t^D}_{xy}}{\partial y} + \frac{\partial {t^D}_{xz}}{\partial z}, \\
\rho\dot{v}_y &= -\frac{\partial p}{\partial y} + \frac{\partial {t^D}_{xy}}{\partial x} + \frac{\partial {t^D}_{yy}}{\partial y} + \frac{\partial {t^D}_{yz}}{\partial z}, \\
\rho\dot{v}_z &= -\frac{\partial p}{\partial z} + \frac{\partial {t^D}_{xz}}{\partial x} + \frac{\partial {t^D}_{yz}}{\partial y} + \frac{\partial {t^D}_{zz}}{\partial z} - \rho g.
\end{aligned} \tag{2.5}$$

In (**6**, **8**), variables are scaled as

$$\begin{aligned}
(x, y) &= [L](\tilde{x}, \tilde{y}), & p &= \rho g[H]\tilde{p}, \\
z &= [H]\tilde{z}, & ({t^D}_{xz}, {t^D}_{yz}, \sigma) &= \epsilon\rho g[H](\tilde{t}^E_{xz}, \tilde{t}^D_{yz}, \tilde{\sigma}), \\
(v_x, v_y) &= [V_L](\tilde{v_x}, \tilde{v_y}), & ({t^D}_{xx}, {t^D}_{yy}, {t^D}_{xy}, {t^D}_{zz}) &= \epsilon^2\rho g[H](\tilde{t}^D_{xx}, \tilde{t}^D_{yy}, \tilde{t}^D_{xy}, \tilde{t}^D_{zz}), \\
v_z &= [V_H]\tilde{v_z}, & \epsilon = [H]/[L] &= [V_H]/[V_L], \\
t &= ([L]/[V_L])\tilde{t}, & F &= [V_L]^2/g[L],
\end{aligned} \tag{2.6}$$

such that dimensionless quantities (denoted by tilde) are of the order of magnitude $\mathcal{O}(1)$, multiplied by typical values (denoted by brackets) $[H]$, $[L]$, $[V_H]$ and $[V_L]$ of height, length, vertical velocity or horizontal velocity, cf (**6**, **8**). The scaling reflects the dominance of the vertical shear stresses t^D_{xz} and t^D_{yz} over the remaining stresses, and which is indeed observed in many parts of an ice sheet, though not everywhere. Inserting (6) into (5) yields

$$\begin{aligned}
\frac{F}{\epsilon}\rho\dot{\tilde{v}}_x &= -\frac{\partial\tilde{p}}{\partial\tilde{x}} + \epsilon^2\frac{\partial\tilde{t}^D_{xx}}{\partial\tilde{x}} + \epsilon^2\frac{\partial\tilde{t}^D_{xy}}{\partial\tilde{y}} + \frac{\partial\tilde{t}^D_{xz}}{\partial\tilde{z}}, \\
\frac{F}{\epsilon}\rho\dot{\tilde{v}}_y &= -\frac{\partial\tilde{p}}{\partial\tilde{y}} + \epsilon^2\frac{\partial\tilde{t}^D_{yy}}{\partial\tilde{y}} + \epsilon^2\frac{\partial\tilde{t}^D_{xy}}{\partial\tilde{x}} + \frac{\partial\tilde{t}^D_{yz}}{\partial\tilde{z}}, \\
F\epsilon\rho\dot{\tilde{v}}_z &= -\frac{\partial\tilde{p}}{\partial\tilde{z}} + \epsilon^2\frac{\partial\tilde{t}^D_{xz}}{\partial\tilde{x}} + \epsilon^2\frac{\partial\tilde{t}^D_{yz}}{\partial\tilde{y}} + \epsilon^2\frac{\partial\tilde{t}^D_{zz}}{\partial\tilde{z}} - 1,
\end{aligned} \tag{2.7}$$

where terms multiplied by powers of ϵ are considered to be small. The Froude number, F, is of the order 10^{-15}, confirming the Stokes assumption, see Section 2.1.

2.2.2 Perturbation Expansion

Each variable $\tilde{q}$ is now expanded in a power series in ϵ, i.e.,

$$\tilde{q} = \sum_{i=0}^{\infty} \epsilon^i \tilde{q}_{(i)}, \tag{2.8}$$

and terms of equal order in ϵ are collected in the scaled equations. This gives rise to a hierarchy of models, named by the highest power of ϵ arising. The classical SIA is obtained

from retaining terms of order ϵ^0 only. A complete model would account for all integer powers of ϵ, and converge towards the solution of the exact equations provided that all terms $\tilde{q}_{(i)}$ are bounded in the whole domain, independently of ϵ. Using this approach, the zeroth order equations (or SIA) equations are derived as

$$\begin{aligned} 0 &= -\frac{\partial \tilde{p}_{(0)}}{\partial \tilde{x}} + \frac{\partial \tilde{t}^D_{xz(0)}}{\partial \tilde{z}}, \\ 0 &= -\frac{\partial \tilde{p}_{(0)}}{\partial \tilde{y}} + \frac{\partial \tilde{t}^D_{yz(0)}}{\partial \tilde{z}}, \\ 1 &= -\frac{\partial \tilde{p}_{(0)}}{\partial \tilde{z}}; \end{aligned} \tag{2.9}$$

the first order (or FOSIA) equations (First Order Shallow Ice Approximation) as:

$$\begin{aligned} 0 &= -\frac{\partial \tilde{p}_{(1)}}{\partial \tilde{x}} + \frac{\partial \tilde{t}^D_{xz(1)}}{\partial \tilde{z}}, \\ 0 &= -\frac{\partial \tilde{p}_{(1)}}{\partial \tilde{y}} + \frac{\partial \tilde{t}^D_{yz(1)}}{\partial \tilde{z}}, \\ 0 &= -\frac{\partial \tilde{p}_{(1)}}{\partial \tilde{z}}; \end{aligned} \tag{2.10}$$

and the second order (or SOSIA) equations as:

$$\begin{aligned} 0 &= -\frac{\partial \tilde{p}_{(2)}}{\partial \tilde{x}} + \frac{\partial \tilde{t}^D_{xz(2)}}{\partial \tilde{z}} + \frac{\partial \tilde{t}^D_{xx(0)}}{\partial \tilde{x}} + \frac{\partial \tilde{t}^D_{xy(0)}}{\partial \tilde{y}}, \\ 0 &= -\frac{\partial \tilde{p}_{(2)}}{\partial \tilde{y}} + \frac{\partial \tilde{t}^D_{yz(2)}}{\partial \tilde{z}} + \frac{\partial \tilde{t}^D_{xy(0)}}{\partial \tilde{x}} + \frac{\partial \tilde{t}^D_{yy(0)}}{\partial \tilde{y}}, \\ 0 &= -\frac{\partial \tilde{p}_{(2)}}{\partial \tilde{z}} + \frac{\partial \tilde{t}^D_{xz(0)}}{\partial \tilde{x}} + \frac{\partial \tilde{t}^D_{yz(0)}}{\partial \tilde{y}} + \frac{\partial \tilde{t}^D_{zz(0)}}{\partial \tilde{z}}. \end{aligned} \tag{2.11}$$

FOSIA models are seldom implemented since they contain, just like the SIA, only the vertical shear stresses, but no normal deviatoric stress or horizontal plane shear stress. However, the FOSIA does account for first order boundary effects and forcings that cannot be represented in SIA (**7**). The earliest appearance of normal deviatoric stresses and the horizontal plane shear stress is in the SOSIA. Although not obvious from (10) and (11), the SOSIA equations include terms of zeroth, first and second order, while the FOSIA equations include terms of zeroth and first order (seen when turning to e.g. the energy equation, the flow law, and equations describing the kinematic boundary conditions at e.g. the ice sheet surface, see (**7**)). One therefore has to solve the SIA equations first, proceed with the FOSIA equations and finally turn to solving the SOSIA equations, presumably improving the accuracy of the solution in each step. Thus, higher order shallow ice approximations can be regarded as an iterative method of solving the full-Stokes equations.

2.2.3 Finite Viscosity Law

It is well known that the expansion procedure yielding the SIA and the SOSIA fails in certain regions of an ice sheet, namely 1) in a marginal boundary strip (though it is argued that failure at the marginal boundary strip is not a complication since the strip is passive and of sub-grid size), 2) close to domes, troughs and ice divides and 3) close to the ice surface. The problems at domes, troughs and near the surface all arise from the singular behaviour of the reciprocal of the creep response function $f(\sigma)^{-1}$ in (3), i.e. that $f(0) = 0$. The singularity means that the viscosity is infinite where the effective stress is zero. In zeroth order, the normal and horizontal plane shear stress t^D_{xx}, t^D_{yy}, t^D_{zz}, t^D_{xy} in (4) are neglected, and thus the effective stress is zero wherever the zeroth order vertical shear stresses are zero, which is at the entire ice surface (**6**, **8**). In the full Stokes setting, normal deviatoric stresses develop (and depending on situation, horizontal plane shear stresses), implying non-zero effective stress at the ice surface except for in a few points. Obviously, the assumption of vertical shear stresses dominating over the normal deviatoric stresses (and horizontal plane shear stress) does not necessarily hold at the ice surface.

Johnson & McMeeking (**12**) therefore proposed that the field variables have to be rescaled in a boundary layer close to the surface, which thickness is denoted by H_{bl}. They conclude that H_{bl} is of $\mathcal{O}(\epsilon^{\frac{1}{3}})$ because the zeroth and second order effective stress behave as $\mathcal{O}((h-z))$ and $\mathcal{O}(\epsilon/(h-z)^2)$, respectively, and thence are of equal size if $h-z = \mathcal{O}(\epsilon^{\frac{1}{3}})$. A continuous solution through the entire ice sheet then requires matching of the solution in the surface boundary layer with the solution outside the layer. The rescaling of variables in a boundary layer is also suggested in Schoof & Hindmarsh (**11**), where the boundary layer is instead defined as the region where t_{xz} and t_{xx} are of equal order of magnitude, yielding similar results as in Johnson & McMeeking (**12**). The rescaling allows for normal deviatoric (and horizontal plane shear) stresses to develop in the boundary layer so that $f \neq 0$ and the singularity in the viscosity is avoided.

Alternatively, a so-called *finite viscosity law* has been suggested, in which a constant σ_{res} is added to f : $f(\sigma) = \sigma^2 + \sigma^2_{res}$ (see e.g. (**14**)). The finite viscosity law corresponds to Newtonian behaviour at low stresses, and is used in the derivation of the SOSIA in Baral et al. (**6**, **7**) to regularise the problem. Non-singular creep functions of non-additive structure have been proposed by e. g. Lliboutry (**13**).

3. Model problem - Ice Flow over a Bumpy Bed

To numerically analyse the foundations of shallow ice approximations, we consider a simple model problem based on the ISMIP-HOM benchmark experiment B (cf. (**22**)), with slight modifications introduced below. Following (**22**), we investigate a diagnostic, isothermal 2D-problem for ice flow over an inclined, bumpy bed, where periodic boundary conditions are applied and no-slip conditions are imposed at the base, see Fig. 1. Further, the rate factor $\mathcal{A}$ is set to 10^{-16} Pa^{-3} a^{-1}, ice density is set to the standard value of 910 $\mathrm{kg/m}^3$, and accumulation and ablation are neglected. The mean ice thickness, $[H]$, is 1000 m and the ice surface, h, and ice base, b, are given by

$$h(x) = -x\tan(\alpha), \quad b(x) = h - [H] + \mu[H]\sin\left(\frac{2\pi}{L}x\right). \tag{3.1}$$

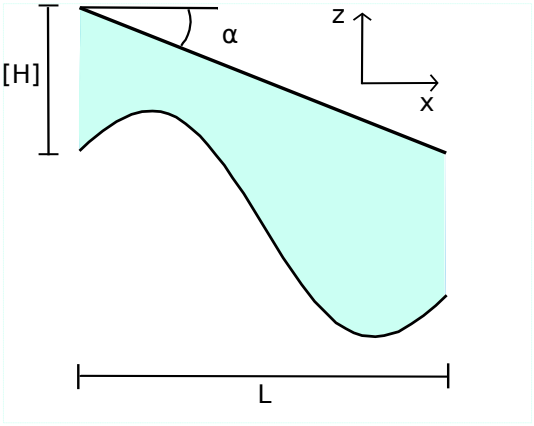

Fig. 1: Model set-up showing the basal topography and the ice surface. The ice flows down-slope in the positive x-direction.

The wavelength of the sinusoidal bumps is thus L m, which corresponds to the typical horizontal extent $[L]$ so that $L = \epsilon[H]$. The amplitude of the bumps is $\mu[H]$ and α the inclination angle of the surface slope. As in (**22**), we vary the wavelength L of the bumps while $[H]$ is kept constant, which corresponds to varying ϵ. However, we consider a larger range of values for L than in the benchmark, namely $L = 10$, 20, 40, 80, 160, 320, 640, 1280, 2560, 5120, and 10240 km, which is equivalent to varying the aspect ratio between $9.77 \cdot 10^{-5}$ and 0.1. We do this in order to investigate the validity of shallow ice approximations in the limit $\epsilon \to 0$. Further, we extend the set-up of the benchmark experiment in that we, in addition to using a constant surface slope inclination angle of 0.5 rad., also let the inclination angle vary with ϵ. Indeed, when non-dimensionalising the ice surface h, viz.

$$\tilde{h}(x) = \frac{h}{[H]} = \frac{-[L]\tilde{x}\tan(\alpha)}{[H]} = \frac{-\tilde{x}\tan(\alpha)}{\epsilon}, \tag{3.2}$$

it becomes obvious that for h to be of $\mathcal{O}(1)$ (and not $\mathcal{O}(\epsilon^{-1})$), $\tan(\alpha)$ should ideally be equal to ϵ and thus, α should be $\arctan\epsilon$ rad.. Similarly, non-dimensionalising the base (with $\alpha = \arctan\epsilon$ rad.) shows that by choosing a constant amplitude μ (i.e. not varying with ϵ), higher order terms arising from the base are avoided:

$$\tilde{b}(x) \quad = \quad \frac{b}{[H]} = \frac{h - [H] + \mu[H]\sin(\omega x)}{[H]} - \tilde{x} - 1 + \mu\sin(2\pi\tilde{x}). \tag{3.3}$$

In summary, if α varies with ϵ, and μ is kept constant, $\tilde{h}$ and $\tilde{b}$ are of $\mathcal{O}(1)$, i.e. only consist of zeroth order terms. In the ISMIP-HOM benchmark μ is 0.5, while we employ up to four different values of μ.

4. Numerical Tests of the Scaling Assumptions

4.1 *Prerequisites and Definition of Boundary Layer*

A meaningful numerical analysis of the quality of different proposed scalings requires a numerical solution that is regarded as the exact one. For the model problem described in Section 3 (i.e. with varying ϵ), we have therefore computed the full Stokes solution using the code Elmer (**24**, **25**). Elmer uses a finite element discretisation of (1) and (2), and for our model problem a structured grid is employed. Further the L_2-norm of a field variable q is computed over the whole domain, ω (with domain volume denoted by V_Ω), and for each ϵ as

$$||q||_2 = \sqrt{\frac{1}{V_\Omega}\int_\Omega q^2 d\Omega}, \tag{4.1}$$

rendering the norm as a function of the aspect ratio. The integral is computed on a discrete grid using the trapezoidal rule. We now write q as

$$q = C\epsilon^\beta(\tilde{q}_{(0)} + \epsilon\tilde{q}_{(1)} + \epsilon^2\tilde{q}_{(2)} + \ldots), \tag{4.2}$$

where C is a constant, and, e.g. $\beta = 1$ for the vertical shear stress and $\beta = 2$ for the normal deviatoric stress according to the scalings in (**7**, **8**) (cf. (6)). Then $q \approx C\epsilon^\beta\tilde{q}_{(0)}$ holds for sufficiently small ϵ, where $\tilde{q}_{(0)}$ is $\mathcal{O}(1)$. Therefore, $||q||_2 \approx C\epsilon^\beta$ for small ϵ.

To estimate C and β from the experiments, we compute the 10-logarithm of the L_2-norm for all $\epsilon \leqslant 1.5625 \cdot 10^{-3}$ ($L = 640$ km). From (16) we get

$$\log_{10}(||q||_2) \approx \log_{10}(C) + \beta\log_{10}(\epsilon). \tag{4.3}$$

To find C and β we fit a linear polynomial to our data for the 10-logarithm of the L_2-norm in the least square sense, using the MATLAB function `polyfit`. In Fig. 2, the black curve shows the logarithm of the L_2-norm for the vertical shear stress, t^D_{xz}, and normal deviatoric stress, t^D_{xx}, respectively (for the surface inclination angle $\alpha = \arctan(\epsilon)$). The pink line is the polynomial fit, which has a slope $\beta = 1$. The 10-logarithm of the L_2-norm is perfectly linear for small ϵ and it is easy to find a polynomial fit. The only data that we find hard to fit a polynomial to, is the quotient between t^D_{xx} and t^D_{xz}, which we will discuss more in Section 4.2. Note that for large ϵ, there is a discrepancy between the data and the polynomial fit, illustrating the role of higher order effects.

Using our numerical experiments, we can also investigate if there is a boundary layer close to the ice surface as discussed in Section 2.2.3, and whether its thickness, denoted H_{bl}, varies as $\mathcal{O}(\epsilon^{\frac{1}{3}})$ as described by Johnson & McMeeking (**12**) and Schoof & Hindmarsh (**11**). We study how the normal deviatoric stress, t^D_{xx}, varies with depth, since this is the field variable that is most sensitive to the high viscosity near the surface. On our discrete grid, the domain is divided into horizontal layers with index k, see Fig. 3a. We denote the positions of the discrete nodes by (x_i, z_k). For each layer k, we compute the sum of the absolute value of the normal deviatoric stress as $\sum_i |t^D_{xx}(x_i, z_k)|$. This sum is large near the ice surface (for large k), and decreases with increasing depth. Obviously, the ice surface is the upper limit of the boundary layer, and we define its lower limit as the depth where $\sum_i |t^D_{xx}(x_i, z_k)|$ amounts to 10 % of the maximum value over all k, see Fig. 3b. This definition was chosen partly for practical reasons. Note that it is not the same definition as in Johnson & McMeeking (**12**) or Schoof & Hindmarsh (**11**). The relation for how H_{bl} varies with ϵ is obtained by fitting a polynomial for $\log_{10}(H_{bl})$ as described above.

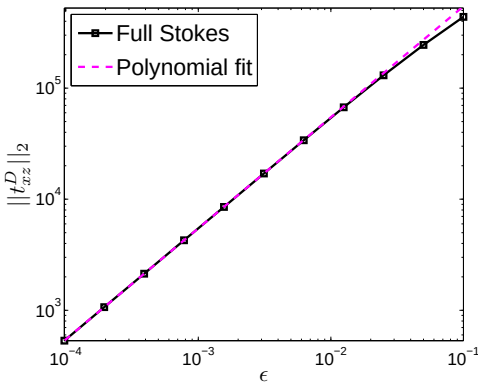

(a) t^D_{xz}. The slope, β, is 1.0.

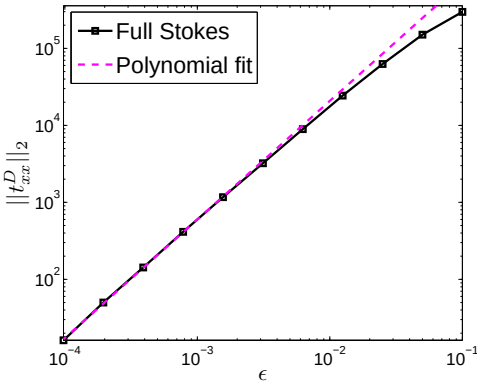

(b) t^D_{xx}. The slope, β, is 1.5.

Fig. 2: The dependence of the norm of the normal deviatoric stress t^D_{xz} and t^D_{xz} on the aspect ratio ϵ, for $\alpha = \arctan(\epsilon)$ and $\mu = 0.5$. The black curve is the results obtained from Elmer while the pink, dashed curve is the polynomial fit.

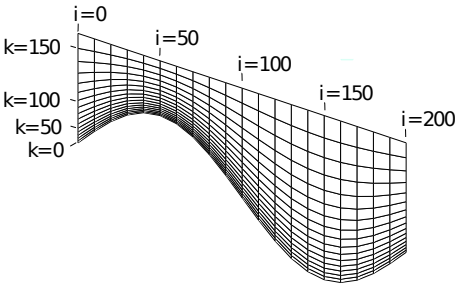

(a) Every tenth mesh-point (x_i, z_k) for a mesh with 160 horizontal layers k, and 200 points in the x-direction.

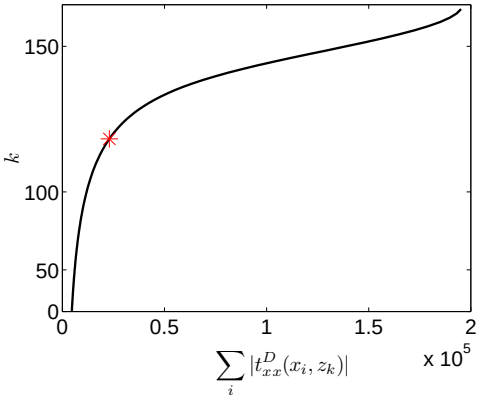

(b) The sum of the normal deviatoric stress at each depth layer k. L is 1280 km. The red star at 10 % of the maximum value marks the border of the boundary layer.

Fig. 3: To define the boundary layer, the sum of the normal deviatoric stress, t^D_{xx} is computed in each horizontal layer, defined by the discrete grid. The resolution of the grid has been varied throughout the work.

Table 1: Theoretical scalings as in Baral et al. (**6**, **8**) and Blatter (**9**) for the whole domain Ω, and as in Schoof & Hindmarsh (**11**) for the inner region, Ω_i and outer region, Ω_o. Note that the theory for how the fractions t^D_{xx}/t^D_{xz} and v_z/v_x behave is not explicitly given in these original sources. $\mathcal{J} = \mathcal{A}[H](\rho g[H])^3 \approx 2.25$ m/s and $\rho g[H] \approx 8.9 \cdot 10^6$ Pa.

Variable	Baral et al. (**6**, **8**)	Blatter (**9**)	Schoof & Hindmarsh (**11**)	
	Total, Ω	Total, Ω	Outer, Ω_o	Inner, Ω_i
t^D_{xx}	$\rho g[H]\epsilon^2$	$\rho g[H]\epsilon^1$	$\rho g[H]\epsilon^2$	$\rho g[H]\epsilon^{4/3}$
t^D_{xz}	$\rho g[H]\epsilon^1$	$\rho g[H]\epsilon^1$	$\rho g[H]\epsilon^1$	$\rho g[H]\epsilon^{4/3}$
p	$\rho g[H]\epsilon^0$	$\rho g[H]\epsilon^1$	$\rho g[H]\epsilon^0$	$\rho g[H]\epsilon^{1/3}$
v_x	-	$\mathcal{J}\epsilon^3$	$\mathcal{J}\epsilon^3$	$\mathcal{J}\epsilon^3$
v_z	-	$\mathcal{J}\epsilon^4$	$\mathcal{J}\epsilon^4$	$\mathcal{J}\epsilon^4$
t^D_{xx}/t^D_{xz}	ϵ^1	1	ϵ^1	1
v_z/v_x	ϵ^1	ϵ^1	ϵ^1	ϵ^1

4.2 *Results*

In this section the numerically computed scaling relations for the field variables t^D_{xz}, t^D_{xx}, p, v_x and v_z are presented in tables. Remember that due to conservation of mass the relation $t^D_{xx} = -t^D_{zz}$ holds in two dimensions and therefore we do not present results for t^D_{zz}. The fractions t^D_{xx}/t^D_{xz} and v_z/v_x are included in the tables, since they are important for the derivation of shallow ice approximations, and since it is not necessarily true that the L_2-norm of a quotient will behave as the quotient of the L_2-norm of the nominator and the L_2-norm of the denominator. To investigate if and how the field variables should be rescaled in a boundary layer close to the ice surface, as proposed in (**11**) and (**12**), we include the scaling of the solution in the whole domain Ω, outside the boundary layer, Ω_o (the *outer solution*), and inside the boundary layer, Ω_i (the *inner solution*) in the tables. We also show how the boundary layer thickness varies with ϵ.

To facilitate comparison, we start by presenting the theoretical scaling relations in Baral et al. (**6**, **8**), Blatter (**9**) and Schoof & Hindmarsh (**11**) in Table 1. The non-uniform scaling in (**11**) depends not only on ϵ, but on an additional parameter λ, which describes the degree of slip at the bed. The scaling relations that apply to our model problem are not explicitly stated in (**11**), but can be obtained considering that we employ no slip conditions and use Glen's flow law with $n = 3$, yielding $\lambda = \epsilon^{-\frac{1}{3}}$. In Schoof & Hindmarsh (**11**) the scaling coincides with Baral et al. (**6**, **8**) outside the boundary layer, but inside it, the variables are rescaled so that the vertical shear stress and the normal deviatoric stress are of equal importance. In both Blatter (**9**) and Schoof & Hindmarsh (**11**) more specific information about the velocities is given than in Baral et al. (**6**, **8**), but the assumption in Baral et al. (**6**, **8**) that $v_z/v_x = \epsilon$ is consistent with the assumptions made in Blatter (**9**) and Schoof & Hindmarsh (**11**). Note that the constant $\mathcal{J}$ is introduced as an abbreviation for $\mathcal{A}[H](\rho g[H])^3$. All stress components and the pressure are assumed to be of equal importance in Blatter (**9**), in contrast to the assumptions in Baral et al. (**6**, **8**). As mentioned in the introduction, the scaling assumptions in Blatter (**9**) yield inconsistent equations, but nonetheless provide a useful model (the Blatter-Pattyn equations), explained in (**11**).

Table 2: The numerically established scaling relations for the boundary layer thickness, field variables and fractions of field variables in the whole domain Ω, in the outer domain Ω_o and in the boundary layer Ω_i. The angle α is constant (0.5 rad.) and the relative bump amplitude $\mu = 0.5$. $\mathcal{J} = \mathcal{A}[H](\rho g[H])^3$.

Variable	Total, Ω	Outer, Ω_o	Inner, Ω_i
H_{bl}	$4.2[H]\epsilon^{0.35}$	-	-
t^D_{xx}	$0.015\rho g[H]\epsilon^{0.46}$	$0.00066\rho g[H]\epsilon^{0.20}$	$0.0087\rho g[H]\epsilon^{0.32}$
t^D_{xz}	$0.0054\rho g[H]\epsilon^{-0.00020}$	$0.010\rho g[H]\epsilon^{0.057}$	$0.024\rho g[H]\epsilon^{0.35}$
p	$0.62\rho g[H]\epsilon^{-6.5\cdot 10^{-6}}$	$1.1\rho g[H]\epsilon^{0.058}$	$2.7\rho g[H]\epsilon^{0.35}$
v_x	$7.1\cdot 10^{-7}\mathcal{J}\epsilon^{-0.0017}$	$4.1\cdot 10^{-7}\mathcal{J}\epsilon^{-0.055}$	$8.0\cdot 10^{-6}\mathcal{J}\epsilon^{-0.0045}$
v_z	$1.2\cdot 10^{-8}\mathcal{J}\epsilon^{-0.0077}$	$1.7\cdot 10^{-8}\mathcal{J}\epsilon^{-0.096}$	$4.9\cdot 10^{-9}\mathcal{J}\epsilon^{-0.016}$
t^D_{xx}/t^D_{xz}	$31\epsilon^{-0.10}$	$0.079\epsilon^{0.14}$	$15\epsilon^{-0.28}$
v_z/v_x	$0.022\epsilon^{0.11}$	$0.014\epsilon^{0.054}$	$0.035\epsilon^{0.16}$

4.2.1 The ISMIP-HOM B set-up: Theoretical vs numerically derived scalings

Table 2 shows the scaling relations obtained by numerically solving the full Stokes equations for the original ISMIP-HOM B benchmark setting, that is, when the angle $\alpha = 0.5$ rad. for all ϵ and $\mu = 0.5$. Our numerical scaling relations obtained for the whole domain Ω should be compared with the uniform scalings in Baral et al. (**6**, **8**) and Blatter (**9**), and our results for Ω_o and Ω_i should be compared with the non-uniform scaling in Schoof & Hindmarsh (**11**). Clearly, the numerically computed scaling relations do not agree with any theory even if the boundary layer is excluded. Two exceptions are the boundary layer thickness H_{bl} and the pressure p. The pressure, considered over the whole domain, agrees well with the uniform scaling in Baral et al. (**6**, **8**). If considered separately in the inner and outer region, respectively, the pressure also agrees fairly well with the theory in Schoof & Hindmarsh (**11**). The boundary layer thickness varies approximately as $\epsilon^{\frac{1}{3}}$ as predicted by Johnson & McMeeking (**12**) and Schoof & Hindmarsh (**11**).

4.2.2 Varying inclination angle

In Section 3 we found that the surface inclination should vary as $\alpha = \arctan(\epsilon)$ rad. in order to avoid terms of $\mathcal{O}(\epsilon^{-1})$ to enter. For this choice of α, the results change dramatically, as shown in Table 3. Considering the whole domain, all field variables, except t^D_{xx}, now agree very well with the theory in Baral et al. (**6**, **8**). Also, we find that the velocities scale approximately as predicted in Blatter (**9**) and Schoof & Hindmarsh (**11**). Regarding the whole domain the normal deviatoric stress t^D_{xx} behaves as $\epsilon^{1.5}$, which corresponds to an intermediate value in the range spanned by the scalings in between the theory in Baral et al. (**6**, **8**) and Blatter (**9**). The constant in the scaling for the fraction t^D_{xx}/t^D_{xz} is very large. Also, as mentioned already before, the polynomial fitting is poor for this fraction.

Considering the boundary layer and the outer region separately, our results agree well with the scalings proposed by Schoof & Hindmarsh (**11**), i.e., the velocities scale similarly both within and outside the boundary layer, while the stresses and the pressure are rescaled within it so that the stresses are of equal order of magnitude. However, the behaviour of t^D_{xx} in the boundary layer spreads to the outer region Ω_o, such that t^D_{xx} varies with ϵ as $\epsilon^{1.7}$

Table 3: The scaling relations for the boundary layer thickness, field variables and fractions of field variables in the whole domain Ω, in the outer area Ω_o and in the boundary layer Ω_i. The inclination angle is $\alpha = \arctan(\epsilon)$ rad. and the relative bump amplitude $\mu = 0.5$. $\mathcal{J} = \mathcal{A}[H](\rho g[H])^3$.

Variable	Total, Ω	Outer, Ω_o	Inner, Ω_i
H_{bl}	$2.7[H]\epsilon^{0.26}$	-	
t^D_{xx}	$2.8\rho g[H]\epsilon^{1.5}$	$1.2\rho g[H]\epsilon^{1.7}$	$1.7\rho g[H]\epsilon^{1.4}$
t^D_{xz}	$0.61\rho g[H]\epsilon^{1.0}$	$1.1\rho g[H]\epsilon^{1.1}$	$1.6\rho g[H]\epsilon^{1.3}$
p	$0.61\rho g[H]\epsilon^{-7.7\cdot 10^{-6}}$	$1.1\rho g[H]\epsilon^{0.054}$	$1.6\rho g[H]\epsilon^{0.26}$
v_x	$1.1\mathcal{J}\epsilon^{3.0}$	$0.53\mathcal{J}\epsilon^{2.9}$	$1.2\mathcal{J}\epsilon^{3.0}$
v_z	$4.9\mathcal{J}\epsilon^{4.0}$	$0.93\mathcal{J}\epsilon^{3.9}$	$4.4\mathcal{J}\epsilon^{4.0}$
t^D_{xx}/t^D_{xz}	$1.6\cdot 10^4\epsilon^{1.1}$	$0.42\epsilon^{0.45}$	$9.8\cdot 10^3\epsilon^{1.0}$
v_z/v_x	$5.6\epsilon^{1.0}$	$2.1\epsilon^{0.92}$	$5.2\epsilon^{0.96}$

instead of ϵ^2 in Ω_o. This is not predicted in Schoof & Hindmarsh (**11**). As mentioned before, our definition of the boundary layer is different from the definition in (**11**). We do not believe that the spreading of the behaviour of t^D_{xx} is due to this difference in definition though, since the boundary layer as defined by us is thick, e.g. for $\epsilon = 10^{-3}$ it is $2.7\cdot 10^3\cdot(10^{-3})^{0.26} \approx 448$ m, i.e. almost 50 % of the mean thickness. Consequently, we do not include regions in the outer region which should have belonged to the inner region and could contaminate our results for the outer region. The spreading is more likely coupled to the fact that even for small ϵ, there is no distinct boundary between the outer and the inner region, cf. Fig. 3b. The polynomial fit for the boundary layer is very good and our result that the boundary layer thickness (and also pressure in the inner domain) varies as $\epsilon^{0.26}$ is considered a fairly good agreement with the theoretical $\epsilon^{\frac{1}{3}}$.

It is interesting that the behaviour of the normal deviatoric stress ($\epsilon^{1.5}$, cf. Table 3) does not agree with theory in Baral et al. (**6**, **8**): ϵ-dependencies should result in consistent equations, and the normal deviatoric stress t^D_{xx} would then necessarily have to vary as ϵ^2 even if the boundary layer is included. Yet, the scaling relation for t^D_{xx} obtained in our experiments is at a first glance *not* consistent with the stress strain relation

$$\frac{\partial v_x}{\partial x} = \mathcal{A} f(\sigma) t^D_{xx}, \tag{4.4}$$

as given by Glen's flow law. We know from our experiments that v_x varies as ϵ^3 and since x varies as L, $\partial v_x/\partial x$ varies as ϵ^4. Furthermore, $\mathcal{A}$ is constant and σ varies as ϵ according to Table 3 (meaning that $f(\sigma)$ should vary as ϵ^2). According to (18) t^D_{xx} then *must* vary as ϵ^2. To understand this mismatch, we have used Elmer to investigate (18) more closely. We rewrite (18) into the form used in Elmer, where the viscosity is expressed in terms of the effective strain d:

$$t^D_{xx} = \mathcal{A}^{-1/3} d^{-2/3} \frac{\partial v_x}{\partial x}, \tag{4.5}$$

where $d = \sqrt{tr(\mathbf{D}^2)/2} = \mathcal{A}\sigma^3$, and $0.5\mathcal{A}^{-1/3}d^{-2/3}$ is the viscosity, η. We are interested in how the ϵ-dependencies in (19) match each other, and have thus investigated the ϵ-dependencies for all components in this (19). The results are presented in Table 4. The

Table 4: The scaling relations for the terms in (19) in the whole domain Ω, in the outer area Ω_o and in the boundary layer Ω_i. The inclination angle is $\alpha = \arctan(\epsilon)$ rad. and the relative bump amplitude $\mu = 0.5$. In the last column the scaling assumptions that are consistent with the scaling of v_x in Blatter (**9**) and Schoof & Hindmarsh (**11**), which are also consistent with our numerical results in Table 3, are given for comparison. $\mathcal{J} = \mathcal{A}[H](\rho g[H])^3$.

Variable	Total, Ω	Outer, Ω_o	Inner, Ω_o	Theory
d	$0.67\frac{\mathcal{J}}{[H]}\epsilon^{3.0}$	$1.6\frac{\mathcal{J}}{[H]}\epsilon^{3.1}$	$1.3\frac{\mathcal{J}}{[H]}\epsilon^{3.8}$	$\frac{\mathcal{J}}{[H]}\epsilon^{3}$
$d^{\frac{2}{3}}$	$0.58\left(\frac{\mathcal{J}}{[H]}\right)^{2/3}\epsilon^{2.0}$	$1.3\left(\frac{\mathcal{J}}{[H]}\right)^{\frac{2}{3}}\epsilon^{2.1}$	$4.5\left(\frac{\mathcal{J}}{[H]}\right)^{\frac{2}{3}}\epsilon^{2.5}$	$\left(\frac{\mathcal{J}}{[H]}\right)^{\frac{2}{3}}\epsilon^{2}$
$d^{-\frac{2}{3}}$	$2.1{\cdot}10^4\left(\frac{\mathcal{J}}{[H]}\right)^{-\frac{2}{3}}\epsilon^{-1.4}$	$0.50\left(\frac{\mathcal{J}}{[H]}\right)^{-\frac{2}{3}}\epsilon^{-2.3}$	$1.3{\cdot}10^4\left(\frac{\mathcal{J}}{[H]}\right)^{-\frac{2}{3}}\epsilon^{-1.5}$	$\left(\frac{\mathcal{J}}{[H]}\right)^{-\frac{2}{3}}\epsilon^{-2}$
$\frac{\partial v_x}{\partial x}$	$6.2\frac{\mathcal{J}}{[H]}\epsilon^{4.0}$	$6.7\frac{\mathcal{J}}{[H]}\epsilon^{4.0}$	$6.2\frac{\mathcal{J}}{[H]}\epsilon^{4.0}$	$\frac{\mathcal{J}}{[H]}\epsilon^{4}$
$d^{-\frac{2}{3}}\frac{\partial v_x}{\partial x}$	$2.51\left(\frac{\mathcal{J}}{[H]}\right)^{\frac{1}{3}}\epsilon^{1.5}$	$1.22\left(\frac{\mathcal{J}}{[H]}\right)^{\frac{2}{3}}\epsilon^{1.7}$	$1.52\left(\frac{\mathcal{J}}{[H]}\right)^{\frac{2}{3}}\epsilon^{1.4}$	$\left(\frac{\mathcal{J}}{[H]}\right)^{\frac{2}{3}}\epsilon^{2}$

theoretical ϵ-dependencies for the effective strain d and $\partial v_x/\partial x$ are obtained from the assumptions in Blatter (**9**) and Schoof & Hindmarsh (**11**), which are consistent with the numerical scaling results of v_x in Table 3. Table 4 shows that d, $d^{2/3}$, and $\partial v_x/\partial x$ behave according to theory. However, going from $d^{2/3}$ to $d^{-2/3}$ does *not* preserve the ϵ-dependencies, nor does multiplication of $d^{-2/3}$ and $\partial v_x/\partial x$ in the boundary layer.

The unexpected behaviour of $d^{-2/3}$ and $d^{-2/3}(\partial v_x/\partial x)$ arises from the fact that the L_2-norm of $d^{-2/3}$ is dominated by regions where d is small (close to the ice surface), contrary to the norm of $d^{2/3}$ which is dominated by regions where d is large (near the ice base). The high values of $d^{-2/3}$, (or viscosity), close to the ice surface result in high values of normal deviatoric stress close to the surface through the stress-strain relations in (18), (19). As for t^D_{xx}, the effect of the different dynamics in the boundary layer for $d^{-2/3}$ spreads to the outer solution. Our finding that $d^{-2/3}(\partial v_x/\partial x)$ behaves as $0.33\epsilon^{1.5}$ is consistent with the result that the normal deviatoric stress behaves as $2.8\rho g[H]\epsilon^{1.5}$, since $\mathcal{A}^{-1/3}d^{-2/3}(\partial v_x/\partial x) = \mathcal{A}^{-1/3}0.33\epsilon^{1.5} = 2.2\cdot 10^7\epsilon^{1.5}$ and $2.8\rho g[H]\epsilon^{1.5} = 2.5\cdot 10^7\epsilon^{1.5}$; thence, the right hand side equals the left hand side in (19). The boundary layer with high viscosities near the ice surface, is thus the reason why t^D_{xx} scales as $\epsilon^{1.5}$ instead of ϵ^2. Even though the stress-strain relation for the vertical shear stress is similar to (19): $t^D_{xz} = 0.5\mathcal{A}^{-1/3}d^{-2/3}\big((\partial v_x/\partial z) + (\partial v_z/\partial x)\big)$, it is not affected by the high viscosity near the ice surface. The explanation is that, unlike $\partial v_x/\partial x$, $\big((\partial v_x/\partial z)+(\partial v_z/\partial x)\big)$ is small at the surface, dampening the influence of the high values of $d^{-2/3}$. Considering the complex behaviour of t^D_{xx}, and the fact that t^D_{xz} is small near the surface explains why it is difficult to fit a polynomial to the fraction t^D_{xx}/t^D_{xz}.

It should be noted that the experiment was repeated with a free surface (i.e. a prognostic experiment), without any change in the conclusions. We also ensured that a sufficiently fine discrete mesh was used in Elmer. The boundary between the inner and outer region was defined as the depth where t^D_{xx} was 10 % of its maximum value. We have tested the sensitivity of our results to different thresholds (5 %, 20 % and 30 %), but the behaviour of t^D_{xx} is the same (there are no changes in the exponent, β, and only slight changes in the

Table 5: Analytically and numerically obtained scaling relations for a flat bed ($\mu = 0$). $1/\sqrt{3} \approx 0.58$, and $\sqrt{8/45} \approx 0.42$. $\mathcal{J} = \mathcal{A}[H](\rho g[H])^3$.

Variable	Analytically	Numerically
t^D_{xx}	$2/\sqrt{3}\rho g[H]\epsilon^2$	$1.12\rho g[H]\epsilon^{2.0}$
t^D_{xz}	$1/\sqrt{3}\rho g[H]\epsilon^1$	$0.57\rho g[H]\epsilon^{1.0}$
p	$1/\sqrt{3}\rho g[H]\epsilon^0$	$0.57\rho g[H]\epsilon^{-0.00041}$
v_x	$\sqrt{8/45}\mathcal{J}\epsilon^3$	$0.43\mathcal{J}\epsilon^{3.0}$
v_z	$\sqrt{8/45}\mathcal{J}\epsilon^4$	$0.43\mathcal{J}\epsilon^{4.0}$
t^D_{xx}/t^D_{xz}	$2\epsilon^1$	$2.0\epsilon^{1.0}$
v_z/v_x	ϵ^1	$1.0\epsilon^{1.0}$

constant). However, H_{bl} varies as $2.7[H]\epsilon^{0.22}$ when 5 % is used and $2.0[H]\epsilon^{0.29}$ when 30 % is used.

4.2.3 Low bump amplitudes

Here we investigate the impact of bump amplitude on the scaling relations. For zero bump amplitude, we can derive an analytical solution to the full Stokes problem which is:

$$t^D_{xz} = \rho g(h-z)\sin(\alpha)\big(\cos^2(\alpha) - \sin^2(\alpha)\big), \tag{4.6}$$

$$t^D_{xx} = 2\rho g(h-z)\sin^2(\alpha)\cos(\alpha), \tag{4.7}$$

$$p = 2\rho g(h-z)\cos(\alpha), \tag{4.8}$$

$$v_x = 0.5\mathcal{A}\cos(\alpha)\big(\rho g\sin(\alpha)\big)^3\big([H]^4 - (h-z)^4\big), \tag{4.9}$$

$$v_z = 0.5\mathcal{A}\sin(\alpha)\big(\rho g\sin(\alpha)\big)^3\big([H]^4 - (h-z)^4\big). \tag{4.10}$$

Since α is small, $\sin(\alpha)$ behaves approximately as $\tan(\alpha) = \epsilon$ and $\cos(\alpha)$ as 1. Thus t^D_{xx} behaves as ϵ^2 for $\mu = 0$. Equation (21) shows that t^D_{xx} is largest at the ice base, and that no boundary layer is present. Even though the viscosity is high near the surface, the normal deviatoric stress is not affected. The reason is that $\partial v_x/\partial x$ vanishes at the surface in (23), dampening the effect of the high viscosity.

We computed the L_2-norm of the field variables for $\mu = 0$ both analytically by applying (15) to (20)-(24) for small ϵ, and numerically in the same manner as when $\mu \neq 0$. The results are presented in Table 5. The numerical and analytical results are in good agreement. All the ϵ-dependencies agree with the theory in Baral et al. (**7**, **8**). Note also that the velocity scaling assumed in Blatter (**9**) and Schoof & Hindmarsh (**11**), $\mathcal{J} = \mathcal{A}[H](\rho g[H])^3$, occurs. Apparently the ϵ-dependencies agree with the ones stated in Baral et al. (**6**, **8**) when $\mu = 0$, but when $\mu = 0.5$, the character of the solution changes: a boundary layer develops and the stresses and pressure scale differently with ϵ.

We now want to know if this transition happens immediately as soon as bump amplitude is larger than zero, or gradually as the amplitude grows. Therefore we perform experiments with $\mu = 0.05$ and $\mu = 0.1$. The results for $\mu = 0.1$ are presented in Table 6, where we see the same rescaling of stresses and pressure in the boundary layer as for $\mu = 0.5$. As when $\mu = 0.5$, the boundary layer effect spreads to the outer solution for t^D_{xx}, which behaves as

Table 6: The scaling relations for the boundary layer thickness, field variables and fractions of field variables in the whole domain Ω, in the outer area Ω_o and in the boundary layer Ω_i. The inclination angle is $\alpha = \arctan(\epsilon)$ rad. and the relative bump amplitude $\mu = 0.1$. $\mathcal{J} = \mathcal{A}[H](\rho g[H])^3$.

Variable	Total, Ω	Outer, Ω_o	Inner, Ω_i
H_{bl}	$2.2[H]\epsilon^{0.31}$	-	-
t^D_{xx}	$1.12\rho g[H]\epsilon^{1.5}$	$0.32\rho g[H]\epsilon^{1.6}$	$0.77\rho g[H]\epsilon^{1.4}$
t^D_{xz}	$0.58\rho g[H]\epsilon^{1.0}$	$0.86\rho g[H]\epsilon^{1.0}$	$1.3\rho g[H]\epsilon^{1.3}$
p	$0.58\rho g[H]\epsilon^{-5.4\cdot 10^{-6}}$	$0.86\rho g[H]\epsilon^{0.036}$	$1.3\rho g[H]\epsilon^{0.30}$
v_x	$0.44\mathcal{J}\epsilon^{3.0}$	$0.35\mathcal{J}\epsilon^{3.0}$	$0.58\mathcal{J}\epsilon^{3.0}$
v_z	$0.71\mathcal{J}\epsilon^{4.0}$	$0.39\mathcal{J}\epsilon^{3.9}$	$0.89\mathcal{J}\epsilon^{4.0}$
t^D_{xx}/t^D_{xz}	$5.1\cdot 10^3\epsilon^{1.1}$	$0.11\epsilon^{0.33}$	$3.4\cdot 10^3\epsilon^{0.90}$
v_z/v_x	$1.5\epsilon^{1.0}$	$1.1\epsilon^{0.97}$	$1.7\epsilon^{0.99}$

$\epsilon^{1.6}$ outside the boundary layer instead of ϵ^2. We see that the constants for t^D_{xz}, t^D_{xx}, v_x and p are the same as for $\mu = 0$ when the whole domain is considered, but even so, t^D_{xx}/t^D_{xz} does not behave nicely, again explained by the boundary layer effect where t^D_{xx} is large where t^D_{xz} is small and vice versa. For $\mu = 0.05$, the ϵ-dependencies for the stresses and pressure are about the same as for $\mu = 0.5$ and $\mu = 0.1$. The development of a boundary layer does thus seem to happen immediately as finite a bump is introduced. The bumps at the bed introduce extra components in $\partial v_x/\partial x$, so that it does not vanish at the surface, and the high viscosity is consequently not dampened. The development of the boundary layer is fast, since only a small extra component in $\partial v_x/\partial x$ is needed for the high viscosity to amplify it. The transition between no boundary layer and a fully developed boundary layer would be more gradual if the non-linearity of the rheology was weaker.

4.2.4 Sensitivity to the finite viscosity parameter $\dot{\gamma}$

As already mentioned, the singularity in Glen's flow law does not introduce singularities in the field variables in the full Stokes setting, but it does give rise to numerical instabilities. To avoid this in Elmer, there is an extra parameter similar to σ_{res}, called the *critical shear rate*, $\dot{\gamma}_o$ (**32**). The critical shear rate provides a lower bound for the *shear rate*, which is related to the effective stress by $\dot{\gamma} = \sqrt{2tr(\mathbf{D}^2)} = 2d = 2\mathcal{A}\sigma^3$. In Elmer, too low a value of $\dot{\gamma}_o$ gives rise to instabilities in t^D_{xz} at the ice surface at $x = L/4$ and $x = 3L/4$ in our model problem. Too high a value alters the rheology and results in too high velocities and a non-smooth, somewhat artificial, appearance of t^D_{xx}. For very small ϵ, it is possible to find an appropriate $\dot{\gamma}_o$ for velocity and stresses simultaneously, but for larger ϵ ($\epsilon \gtrsim 1/1280$) we could not find any. For $\mu = 0.5$ we have used a small, constant, $\dot{\gamma}_o$ equal to 10^{-10}. To make sure that our choice of $\dot{\gamma}_o$ is not erroneously influencing our numerical scaling relations we did a sensitivity study including a number of constants multiplied with ϵ^0 and ϵ^3, respectively. Note that the latter ϵ-dependence is consistent with $t^D_{xx} \sim \epsilon^2$. Except for H_{bl} behaving as $\epsilon^{0.28}$ instead of $\epsilon^{0.26}$, this did *not* alter the ϵ-dependencies in Table 3. Maybe not so surprising, the influence of $\dot{\gamma}_o$ is coupled to bump amplitude. For $\mu = 0.1$ and $\mu = 0.05$ we had to lower the critical shear rate, since the boundary layer and t^D_{xx} was

affected for small ϵ when $\dot{\gamma}_o = 10^{-10}$ was used. For $\mu = 0$, when there was no boundary layer, the problem appeared to be insensitive to $\dot{\gamma}_0$.

Out of curiosity, we also tried setting $\dot{\gamma}_o$ as a large constant multiplied by ϵ in hope of regularising the problem and reducing the boundary layer effect, which indeed was the result. The rheology is then altered such that the scaling relations agree more with Baral et al. (**6**, **8**) than with Schoof & Hindmarsh (**11**).

5. The Second Order Shallow Ice Approximation

The SOSIA for non-Newtonian ice, as described in (**6**), has never before been implemented. It was applied by Mangeney & Califano (**28**) for Newtonian, anisotropic ice, and recently by Egholm et al. (**29**), though not in its pure form but in a depth-averaged, iterative scheme. In the previous section we studied the behaviour of the full Stokes solution and the appropriateness of the assumptions, i.e. the scaling relations in Baral et al. (**6**, **7**, **8**), in the derivation of SIA and SOSIA. We are thus ready to proceed to a more direct analysis of the SIA and SOSIA equations, as they are described in (**6**, **7**). We solve them both analytically and numerically for the model problem in Section 3. We first present the equations, then the analytical solutions, which illustrate important properties of the shallow ice approximations, and then the numerical results.

5.1 *The (Integrated) SOSIA-equations for the ISMIP-HOM B experiment*

The second order variables $t_{xz(2)}$, $p_{x(2)}$ and $v_{x(2)}$ for the model problem are given here, together with the zeroth order expressions for completeness of presentation. The z-velocity is excluded for brevity of presentation, since it follows from the mass balance in the same way for all orders. The model problem simplifies the equations considerably since it includes neither higher order boundary terms, y-dependency, temperature variations, nor sliding at the base (in fact (25)-(29) holds for all such problems). The well-known zeroth order expressions, denoted by subscript (0), for shear stress and velocity are

$$t^D_{xz(0)} = -\rho g \frac{\partial h_{(0)}}{\partial x}(h_{(0)} - z), \quad v_{x(0)} = 2\rho g \frac{\partial h_{(0)}}{\partial x} \int_{b_{(0)}}^{z} \mathcal{A}f(\sigma_{(0)})(h_{(0)} - z')dz'. \tag{5.1}$$

In order to compute $t_{xz(2)}$ from (11) we need the zeroth order normal deviatoric stresses (and depending on situation, horizontal plane shear stress), which are not computed in zeroth order approximation as they are not needed for the zeroth order velocities. The normal deviatoric stress in the x-direction is given directly by the stress-strain relation in (**6**, **8**):

$$t^D_{xx(0)} = \frac{1}{\mathcal{A}f(\sigma_{(0)})} \frac{\partial v_{x(0)}}{\partial x}. \tag{5.2}$$

As mentioned before, $t_{xx} = -t_{zz}$, and $t_{xy} = 0$ for the 2D case. The shear stress, pressure and the horizontal velocity are obtained from the horizontal momentum balance, vertical momentum balance and stress strain relation, respectively, where they occur in derivatives.

It is customary to vertically integrate the SIA-equations in order to avoid having to solve for the variables numerically. This is also convenient for the SOSIA. In (**6**, **8**), the vertical integration is carried out for the shear stresses and the pressure only, and the resulting expressions are presented in (27), (28) (with misprints in (**6**) corrected). Going beyond the

results of (**6**), we derive here also the second order velocity, $v_{x(2)}$ in (29), computed from the stress-strain relation and boundary conditions at the base.

$$\epsilon^2 p_{(2)} = \rho g \frac{1}{2}\left(h_{(0)}-z\right)^2 \frac{\partial^2 h_{(0)}}{\partial x^2} + \rho g \left(h_{(0)}-z\right)\left(\frac{\partial h_{(0)}}{\partial x}\right)^2 + t^D_{zz(0)}. \tag{5.3}$$

$$\begin{aligned}\epsilon^2 t^D_{xz(2)} &= -\rho g \frac{\partial}{\partial x}\left(-\frac{1}{6}(z-h_{(0)})^3 \frac{\partial^2 h_{(0)}}{\partial x^2} h_{(0)} + \frac{1}{2}\left(z-h_{(0)}\right)^2 \left\|\nabla_H h_{(0)}\right\|^2\right) \\ &- \frac{\partial}{\partial x}\int_z^{h_{(0)}} t^D_{zz(0)} dz' + \frac{\partial}{\partial x}\int_z^{h_{(0)}} t^D_{xx(0)} dz'.\end{aligned} \tag{5.4}$$

$$\begin{aligned}v_{x(2)} &= -\frac{1}{\epsilon^2}\frac{\partial}{\partial x}\int_{b_{(0)}}^z v_{z(0)} dz + 6\mathcal{A}\int_{b_{(0)}}^z {t^D_{xz(0)}}^2 t^D_{xz(2)} dz' + \\ &+ \frac{2}{\epsilon^2}\mathcal{A}\int_{b_{(0)}}^z t^D_{xz(0)} {t^D_{xx(0)}}^2 dz' + 2\sigma^2_{res}\mathcal{A}\int_{b_{(0)}}^z t^D_{xz(2)} dz'\end{aligned} \tag{5.5}$$

5.2 *Analytical Solutions for the Zeroth and Second Order Shallow Ice Approximation*

Equations (27)-(29) yield explicit expressions for second order variables. For the geometry in Section 3 we have computed the integrals and derivatives in these expressions and thus obtained analytical solutions to the SOSIA. To avoid infinite viscosities, we have followed the suggested regularisation in Baral et al. (**6**), i.e. adding a constant to the creep response function, $f(\sigma) = \sigma^2 + \sigma^2_{res}$. The solutions are expressed in terms of the inclination angle of the ice surface α, relative amplitude μ, finite viscosity parameter σ_{res} and wavelength L. In the appendix the same solutions are expressed terms of h, b and H instead. By (25), the zeroth order shear stress is

$$t^D_{xz(0)} = -\rho g \tan(\alpha)(x\tan(\alpha) + z). \tag{5.6}$$

The zeroth order velocity in (25) is given by

$$\begin{aligned}v_{x(0)} &= 2\rho g \mathcal{A}\tan(\alpha)\left(\frac{(\rho g \tan(\alpha))^2}{4}\left(\ [H]^4\left(1-\mu\sin\left(2\pi x/L\right)\right)^4 - \left(x\tan(\alpha)+z\right)^4\right)\right. \\ &+ \left.\frac{\sigma^2_{res}}{2}\left([H]^2\left(1-\mu\sin\left(2\pi x/L\right)\right)^2 - \left(x\tan(\alpha)+z\right)^2\right)\right).\end{aligned} \tag{5.7}$$

The magnitude of the velocity does not depend on L, but it does depend on the relative amplitude μ. Also, there is an extra term stemming from the finite viscosity law with $\sigma_{res} > 0$. Technically, a finite viscosity law is not needed for the zeroth order model, since the creep response function never appears in the denominator; however, it becomes necessary when continuing to second order. To calculate second order shear stress and velocity, the zeroth order normal deviatoric stress in (26) is needed, given by

$$t^D_{xx(0)} = -2\rho g \tan^2(\alpha)(x\tan(\alpha) + z) \tag{5.8}$$

$$
\begin{aligned}
&- \quad \frac{4\pi}{L}\rho g[H]^2\mu\tan(\alpha)\frac{\cos\left(2\pi x/L\right)\left(1-\mu\sin\left(2\pi x/L\right)\right)}{\left(\left(\left(x\tan(\alpha)+z\right)\tan(\alpha)\right)^2+\left(\frac{\sigma_{res}}{\rho g}\right)^2\right)} \\
&\cdot \quad \left(\tan^2(\alpha)[H]^2\left(1-\mu\sin\left(2\pi x/L\right)\right)^2+\left(\frac{\sigma_{res}}{\rho g}\right)^2\right).
\end{aligned}
$$

Having calculated $t^D_{xx(0)}$, the second order shear stress is computed from (28) as

$$
\begin{aligned}
\epsilon^2 t^D_{xz(2)} &= 3\rho g\tan^3(\alpha)(x\tan(\alpha)+z) \\
&+ 8\rho g[H]^2\frac{\pi}{L}\mu\tan^2(\alpha)\frac{\left(1-\mu\sin\left(2\pi x/L\right)\right)\cos\left(2\pi x/L\right)}{\tan^2(\alpha)(x\tan(\alpha)+z)^2+\frac{\sigma^2_{res}}{(\rho g)^2}} \\
&\cdot \quad \frac{\left([H]^2\tan^2(\alpha)\left(1-\mu\sin\left(2\pi x/L\right)\right)^2+\frac{\sigma^2_{res}}{(\rho g)^2}\right)}{\tan^2(\alpha)(x\tan(\alpha)+z)^2+\frac{\sigma^2_{res}}{(\rho g)^2}} \\
&- \quad \frac{4(\rho g)^2[H]^2}{\sigma_{res}}\left(\frac{2\pi}{L}\right)^2\mu\Big(3[H]^2\left(1-\mu\sin\left(2\pi x/L\right)\right)^2\mu\cos^2\left(2\pi x/L\right)\tan^2(\alpha) \\
&+ \quad [H]^2\left(1-\mu\sin\left(2\pi x/L\right)\right)^3\sin\left(2\pi x/L\right)\tan^2(\alpha) \\
&+ \quad \frac{\sigma^2_{res}}{(\rho g)^2}\left(\mu\cos^2\left(2\pi x/L\right)+\left(1-\mu\sin\left(2\pi x/L\right)\right)\sin\left(2\pi x/L\right)\right)\Big) \\
&\cdot \quad \arctan\left(\rho g\frac{\tan(\alpha)(x\tan(\alpha)+z)}{\sigma_{res}}\right).
\end{aligned}
\tag{5.9}
$$

An explicit dependence on L is introduced in (32)-(33), and hence on the aspect ratio ϵ. Also, (32) and (33) depend on α, μ and σ_{res}. In $t^D_{xx(0)}$, σ_{res} appears in the denominator, preventing singularities to occur at the ice surface when z is equal to $h=-x\tan(\alpha)$, see (32). The expression for $t^D_{xz(2)}$ illustrates the difficulties in choosing an appropriate σ_{res}, as σ_{res} appears both in the nominator and denominator and hence must neither be chosen too large, nor too small in (33). Having $t^D_{xx(0)}$ and $t^D_{xz(2)}$, the second order velocity can be derived from (29). The expression for the second order solution is very long and is included in the appendix for the interested reader. In fact it behaves similarly to the second order shear stress, where σ_{res} appears both in the nominator and denominator. Remember that to get the full second order solution, the zeroth and second order contributions should be added together as $v_x = v_{x(0)} + \epsilon^2 v_{x(2)}$. The extra term arising from the finite viscosity law in $v_{x(0)}$ in (31) is quite large, and thus the SOSIA velocity does not allow too large a σ_{res}. The SOSIA shear stress is not as sensitive to large σ_{res}, since the zeroth order shear stress in (30) does not contain any terms from the finite viscosity law. However, because there are large terms where σ_{res} is in the denominator, it does not allow σ_{res} to be too small. Note that all terms involving σ_{res} are pre-multiplied with μ; thus, for decreasing μ the influence of σ_{res} decays. This agrees with our finding in Section 4, that the boundary layer near the ice surface disappears when $\mu = 0$ at the same time as the sensitivity to the finite viscosity parameter in Elmer, $\dot{\gamma}_0$, diminishes.

The SOSIA-equations are derived assuming that the scaling relations in Baral et al. (**6**, **8**) hold, and we expect the second order expressions to fulfil these scaling relations as well.

The analytical solutions clearly show how α, μ, and σ_{res} should depend on the aspect ratio to achieve this. We know that, according to Baral et al. (**6**, **8**), the shear stress should depend linearly on ϵ, the normal deviatoric stress should depend quadratically on ϵ and that the x-velocity divided by the z-velocity should vary linearly with ϵ. The analytical solution has the correct dependence on the aspect ratio provided that $\tan(\alpha)$ and σ_{res} vary linearly in ϵ, and if μ is independent of ϵ (for α, μ this was also the conclusion in Section 3). Inserting $\tan(\alpha) = \epsilon$ (as in Section 3) and $\sigma_{res} = C_\sigma \rho g[H]\epsilon$ (resembling the scaling of σ, see (6)) in (30)-(33) yields:

$$t^D_{xz(0)} = -\rho g[H]\epsilon(\tilde{x} + \tilde{z}), \tag{5.10}$$

$$\begin{aligned} v_{x(0)} &= \mathcal{A}[H](\rho g[H])^3\epsilon^3 \left(\frac{1}{2}(1 - \mu\sin(2\pi\tilde{x}))^4\right. \\ &- \left.\frac{1}{2}(\tilde{x} + \tilde{z})^4 + C_\sigma^2(1 - \mu\sin(2\pi\tilde{x}))^2 - C_\sigma^2\frac{1}{2}(\tilde{x} + \tilde{z})^2\right), \end{aligned} \tag{5.11}$$

$$\begin{aligned} t^D_{xx(0)} &= -\rho g[H]\epsilon^2\frac{2}{(\tilde{x} + \tilde{z})^2 + C_\sigma^2}\Big((\tilde{x} + \tilde{z})((\tilde{x} + \tilde{z})^2 + C_\sigma^2)\Big. \\ &- \Big. 2\pi\mu\cos(2\pi\tilde{x})(1 - \mu\sin(2\pi\tilde{x}))((1 - \mu\sin(2\pi\tilde{x})) + C_\sigma^2)\Big), \end{aligned} \tag{5.12}$$

$$\begin{aligned} \epsilon^2 t^D_{xz(2)} &= \rho g[H]\epsilon^3\Big(3(\tilde{x} + \tilde{z}) \\ &+ 8\pi\mu\frac{(1 - \mu\sin(2\pi\tilde{x}))\cos(2\pi\tilde{x})\big((1 - \mu\sin(2\pi\tilde{z}))^2 + C_\sigma^2\big)}{(\tilde{x} + \tilde{z})^2 + C_\sigma^2} \\ &- 16\pi^2\frac{\mu}{C_\sigma}\Big(3\mu(1 - \mu\sin(2\pi\tilde{x}))^2\cos^2(2\pi\tilde{x}) + (1 - \mu\sin(2\pi\tilde{x}))^3\sin(2\pi\tilde{x}) \\ &+ C_\sigma^2\Big(\mu cos^2(2\pi\tilde{x}) + (1 - \mu\sin(2\pi\tilde{x}))\sin(2\pi\tilde{x})\Big)\Big)\arctan\left(\frac{\tilde{x} + \tilde{z}}{C_\sigma}\right)\Big), \end{aligned} \tag{5.13}$$

where $\tilde{x}$ and $\tilde{z}$ are the non-dimensionalised x- and z-coordinates. The expressions in (34)-(37) only depend on geometry, material constants, and C_σ. In line with (6), $t^D_{xz(0)}$ is pre-multiplied by $\rho g[H]\epsilon$, $t^D_{xx(0)}$ is pre-multiplied by $\rho g[H]\epsilon^2$ and $\epsilon^2 t^D_{xz(2)}$ is pre-multiplied by $\rho g[H]\epsilon^3$. Note that the multiplying factor in $v_{x(0)}$ is $\mathcal{A}[H](\rho g[H])^3\epsilon^3 (= \mathcal{J}\epsilon^3)$ as in Blatter (**9**) and Schoof & Hindmarsh (**11**). In the same manner, the analytical solution for $v_{z(0)}$ (which is not given here for brevity of presentation) is multiplied by $\mathcal{A}[H](\rho g[H])^3\epsilon^4$.

As already discussed σ_{res} appears in the nominator in some of the equations, while it occurs in the denominator in others. It is reasonable to require that the relative effect of σ_{res}, or C_σ, should be approximately the same for all field variables. Since the zeroth order effective stress is low near the surface, σ_{res} is the most influential there. To estimate the magnitude of C_σ we therefore simplify the above equations by only considering the ice surface, i.e. when $\tilde{x} + \tilde{z} = 0$. Setting the relative effect of C_σ at the surface for $v_{x(0)}$ (where C_σ appears in the nominator and should ideally be zero) equal to the relative effect of C_σ

at the surface for $t^D_{xx(0)}$ (where C_σ is in the denominator) we derive a value for C_σ. At the surface, $v_{x(0)}$ and $t^D_{xx(0)}$ are

$$v_{x(0)} = \mathcal{A}[H](\rho g[H])^3\epsilon^3\left(\left(1-\mu\sin(2\pi\tilde{x})\right)^2 \quad \left(\frac{1}{2}\left(1-\mu\sin(2\pi\tilde{x})\right)^2 + C_\sigma^2\right)\right), \tag{5.14}$$

and

$$t^D_{xx(0)} = \rho g[H]\epsilon^2 4\pi\mu\cos(2\pi\tilde{x})\left(1-\mu\sin(2\pi\tilde{x})\right)\left(\frac{\left(1-\mu\sin(2\pi\tilde{x})\right)}{C_\sigma^2}+1\right). \tag{5.15}$$

We compute the ratio of term involving C_σ to the total expression for $v_{x(0)}$, and set it equal to the corresponding fraction for $t^D_{xx(0)}$, yielding:

$$\frac{C_\sigma^2}{\frac{1}{2}\left(1-\mu\sin(2\pi\tilde{x})\right)^2 + C_\sigma^2} = \frac{\left(1-\mu\sin(2\pi\tilde{x})\right)^2}{\left(1-\mu\sin(2\pi\tilde{x})\right)^2 + C_\sigma^2} \tag{5.16}$$

To measure the *average* relative effect at the ice surface, not the effect at a specific point, we replace $\left(1-\mu\sin(2\pi\tilde{x})\right)^2$ by its mean

$$\overline{\left(1-\mu\sin(2\pi\tilde{x})\right)^2} = \int_0^1 \left(1-\mu\sin(2\pi\tilde{x})\right)^2 d\tilde{x} = 1+\frac{\mu^2}{2}, \tag{5.17}$$

resulting in

$$C_\sigma^2 = \frac{1}{\sqrt{2}}\left(1+\frac{\mu^2}{2}\right). \tag{5.18}$$

Equation (42) illustrates that the importance of C_σ grows with growing amplitudes. The sensitivity of SOSIA to σ_{res} is investigated further by numerical experiments in Section 5.4.

5.3 *Implementation of SOSIA*

Our implementation of the SOSIA equations follows the standard in SICOPOLIS (**30**). Finite differences are used on a staggered grid for stability reasons. The velocities, horizontal volume fluxes, vertical shear stresses and the horizontal derivatives of bedrock topography and ice-surface topography are defined in between the grid points. All other quantities are defined at grid points. When a quantity is needed in a point where it is not defined, linear interpolation is used. To ensure that the grid points coincide with physical boundaries, a σ-transformation is used, see e.g. (**31**). Central differences are applied when it is possible, otherwise one sided differences is used. Integrals are computed by the trapezoidal method if the integrand and the integral are defined at the same points. If the integrand and the integral are defined at different points (one in between grid points and one at grid points), the midpoint rule is used instead.

5.4 *Numerical results and sensitivity to σ_{res}*

We have applied the SIA and the SOSIA for the problem described in Section 3, with L varying between 10 and 10240 km. We measure the accuracy of SIA and SOSIA for each

L (i.e. ϵ) by comparing to the full Stokes solution provided by Elmer. All our results presented in this section will regard the accuracy for the x-velocity v_x and shear stress t^D_{xz}. The reason for this is that the normal deviatoric stresses t^D_{xx} and t^D_{zz} are not calculated to second order, since this is not necessary to obtain the velocity field, and the z-velocity is excluded for the same reasons as in Section 5.1. The accuracy is measured in the L_2-norm in (15) in terms of the relative difference

$$\frac{||q_{x,fullStokes} - q_{x,SIA/SOSIA}||_2}{||q_{x,fullStokes}||_2}, \tag{5.19}$$

where q is v_x or t^D_{xz}. For a fair analysis of the accuracy of the SOSIA, we must know how to choose the finite viscosity parameter σ_{res}, as we know from our analytical solutions that the second order contribution is very sensitive to this parameter. In Baral et al. (**6**), $\sigma_{res} = \sqrt{10^9}$ is used for the Greenland ice sheet, but with no explanation of this choice. Our analytical solutions suggest that σ_{res} should vary with ϵ as $C_\sigma \rho g[H]\epsilon$, and that the value of C_σ should be about $C_\sigma^2 = 1/\sqrt{2}\left(1 + \mu^2/2\right)$, see (42). In our numerical experiments, we vary C_σ to see how the accuracy of SOSIA depends on it. Baral et al. (**6**) suggested that σ_{res} should be added everywhere (i.e. in the whole domain), as in the analytical solution. We use both this formulation and experiment with σ_{res} as a lower bound on the effective stress, viz:

$$\sigma = \max(\sigma_{(0)}, \sigma_{res}), \tag{5.20}$$

and compare with the result when adding it everywhere. The choice (44) is more similar to the way that infinite viscosity is handled in Elmer. By not adding σ_{res} everywhere the total influence of σ_{res} is smaller.

5.4.1 High bump amplitude, $\mu = 0.5$

We know from Section 4 that if the surface inclination angle, α, does not vary with ϵ, the shallow ice approximation theory does not hold at all. Therefore we have measured the accuracy for the case $\alpha = \arctan(\epsilon)$ rad., $\mu = 0.5$, first with σ_{res} added everywhere (Fig. 4a, Fig. 4b) and second with σ_{res} acting as a lower bound on the effective stress (Fig. 5).

The accuracy of the SIA is measured with $C_\sigma = 0$, since a finite viscosity law is unnecessary in this case. According to theory, the error should be of $\mathcal{O}(\epsilon^2)$. As seen in e.g. Fig. 4a, the relative error in the SIA velocity only decreases around 1.5 order of magnitudes when ϵ decreases from 10^{-1} to 10^{-3}, thus the error decays faster than ϵ^1, but slower than the theoretical ϵ^2. The accuracy of the vertical shear stress is even further from $\mathcal{O}(\epsilon^2)$. This suggests that the correction terms are not of second order. The mismatch between theoretical accuracy and our results is not surprising considering that the scaling assumption in Baral et al. (**6**, **8**) is not fully appropriate for a bumpy bed, as seen in Section 4. As for the accuracy of SOSIA, we have assessed it for $C_\sigma = 0.11$, $C_\sigma = 0.35$ and $C_\sigma = 1.12$. The value given by (42), only considering the ice surface, is 0.89. Fig. 4 and Fig. 5 shows that the velocity is more sensitive to σ_{res} than the shear stress.

There are two types of errors in the SOSIA solution. One is due to the extra zeroth order term in the velocity introduced by the finite viscosity law in (31). Since there is no such zeroth order term in the vertical shear stress, only the velocity is affected by this type of error. The zeroth order term involving σ_{res} is dominant for small ϵ if C_σ is too large (see

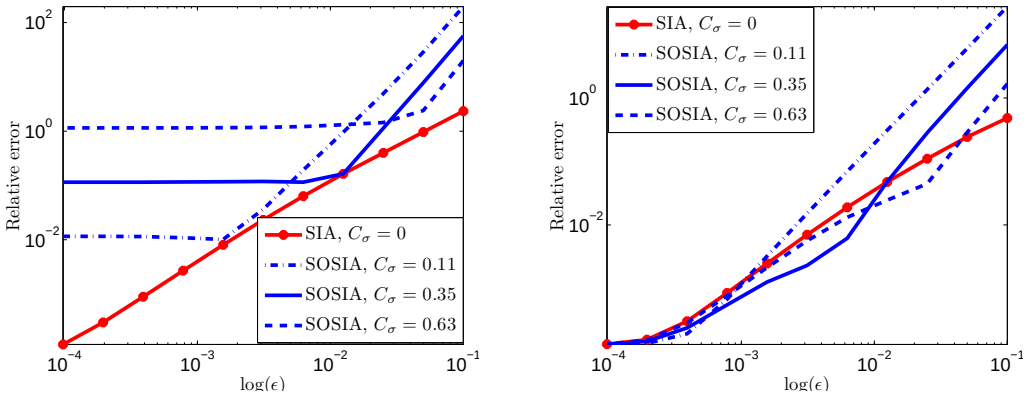

(a) v_x. (b) t^D_{xz}.

Fig. 4: Relative error in x-velocity and vertical shear stress, for the SIA and SOSIA. For SOSIA, $\sigma_{res} = C_\sigma \rho g[H]\epsilon$ is added everywhere.

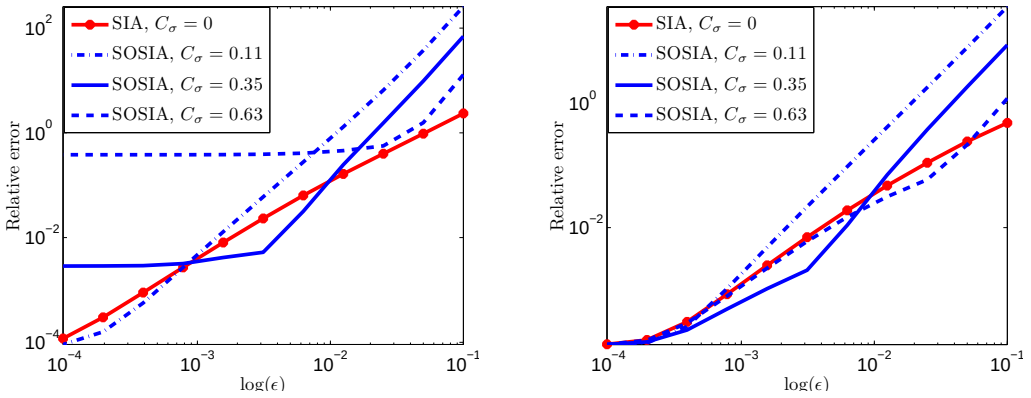

(a) v_x. (b) t^D_{xz}.

Fig. 5: Relative error in x-velocity and vertical shear stress, for the SIA and SOSIA. For SOSIA, $\sigma_{res} = C_\sigma \rho g[H]\epsilon$ is a lower threshold for the effective stress.

Fig. 6 when $C_\sigma = 1.12$). The extra zeroth order term in the velocity also causes the SOSIA velocity to be less accurate than SIA for all ϵ when σ_{res} is added to the creep response function everywhere, regardless of the value of C_σ. Using σ_{res} as a smaller threshold of the effective stress instead, the influence of the zeroth order term is decreased, see Fig. 5a and Fig. 5b.

The other type or error is a dip in the velocity and vertical shear stress caused by the non-linear, singular behaviour of Glen's flow law. This type of error is dominant when ϵ is large and σ_{res} is too small, see Fig. 6 for $C_\sigma = 0.11$ and Fig. 7a. The dip occurs around $x = 3L/4$, where the normal deviatoric stress is zero at the surface in both the SOSIA (see (39)) and full Stokes setting.

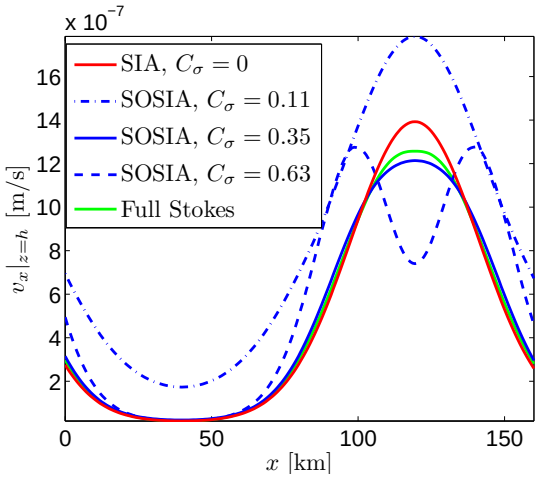

Fig. 6: Surface x-velocity for $L = 160$ km from the full Stokes solution, the SIA and the SOSIA. For SOSIA, $\sigma_{res} = C_\sigma \rho g[H]\epsilon$ is used as a lower threshold for the effective stress.

If σ_{res} is added everywhere in the whole domain, the two types of errors overlap each other, so that there is no value of σ_{res} and ϵ for which the SOSIA error is smaller than the SIA error. When σ_{res} is used as a threshold, there are cases when the SOSIA improves the SIA, see Fig. 5. Choosing C_σ as 0.35, the SOSIA surface velocity is closer to the full Stokes solution than SIA when $\epsilon = 1/160, 1/320, 1/640$. Fig. 7b shows how this choice of C_σ reduces the overestimation in the SIA velocity at $x = 3L/4$ when $L = 320$ km. For larger ϵ than about $1/160$, the SOSIA is much worse than the SIA, and for smaller ϵ than about $1/640$, the SIA is slightly more accurate than the SOSIA, but here the error is so small that it is negligible. Note that according to the theory in (**6**) SOSIA should be more accurate than SIA for all $\epsilon < 1$.

Apparently $C_\sigma = 0.35$ is the best choice out of the constant values that we tried, but Fig. 4a and Fig. 5a suggests that the optimal C_σ is *not* independent of ϵ. Indeed, if we choose $C_\sigma = 4\sqrt{\epsilon}$ the interval where the SOSIA velocity error is smaller than the SIA velocity error is larger than $[1/640, 1/160]$, which was obtained for $C_\sigma = 0.35$. However, an ϵ-dependent C_σ is in conflict with the analytical solutions suggesting that C_σ should be a constant.

5.4.2 Low bump amplitude, $\mu = 0.1$

In Section 4 we found that there is a boundary layer close to the ice surface when there are bumps at the bed, in which the assumptions in Baral et al. (**6**, **8**) does not hold. In Section 5.2 we derived analytical solutions for the SOSIA and concluded that the effect of σ_{res} is higher when μ is large (see (42)). This suggests that SOSIA might be more accurate for lower bump amplitudes. We have applied the SIA and SOSIA for $\mu = 0.1$, and the result is illustrated in Fig. 8, which displays the accuracy of v_x and t^D_{xz}. The accuracy of SIA is slightly higher than for $\mu = 0.5$, but still it does not behave as ϵ^2. As $C_\sigma = 1.12$ is much too large in this case, Fig. 8 displays of SOSIA for $C_\sigma = 0.11$, $C_\sigma = 0.35$ and $C_\sigma = 0.63$.

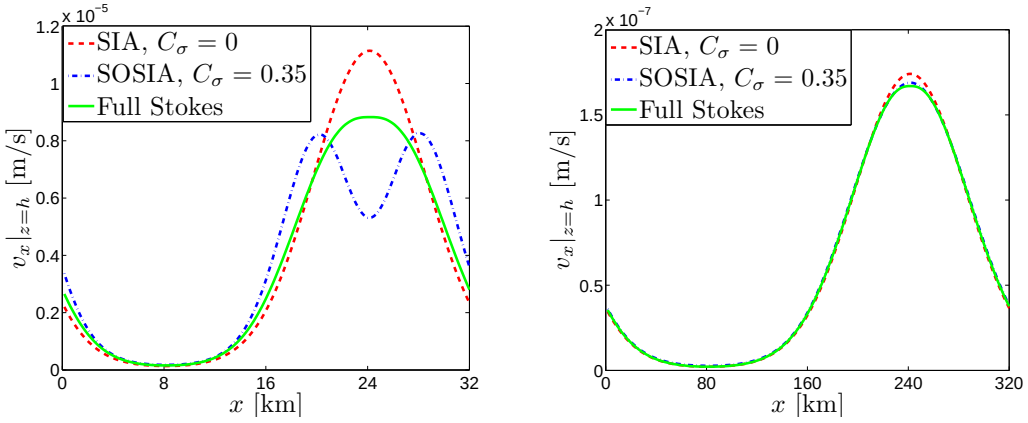

(a) $L = 80$ km. (b) $L = 320$ km.

Fig. 7: Surface x-velocity for the full Stokes solution, the SIA and the SOSIA. For SOSIA, $\sigma_{res} = C_\sigma \rho g[H]\epsilon$ is used as a lower threshold for the effective stress and $C_\sigma = 0.35$.

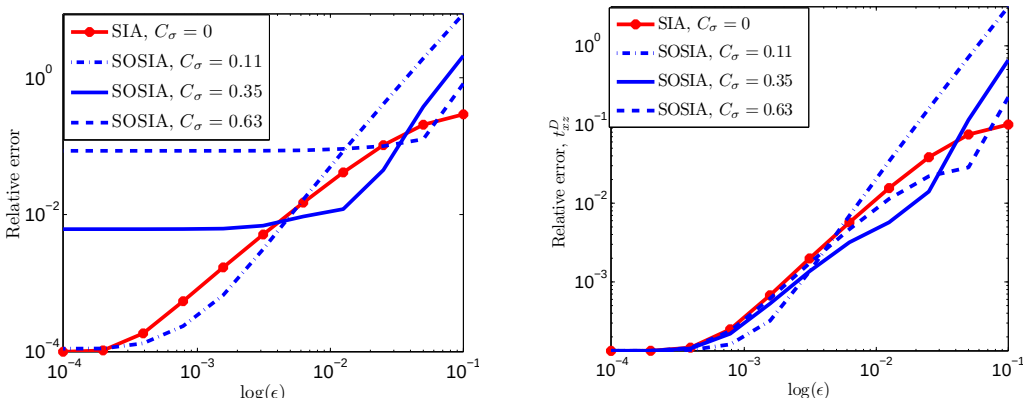

(a) v_x. (b) t^D_{xz}.

Fig. 8: Relative error in x-velocity and vertical shear stress for the SIA and SOSIA. For SOSIA, $\sigma_{res} = C_\sigma \rho g[H]\epsilon$ is a lower threshold for the effective stress.

The same overall behaviour is seen as when $\mu = 0.5$, but the accuracy of the second order velocity is higher for $\mu = 0.1$ than it is for $\mu = 0.5$ and the sensitivity to the choice of C_σ is slightly less severe, as expected from (38) and (42). Note that for all experiments with SIA and SOSIA, including those for $\mu = 0.5$, we ensured that a sufficiently fine discrete mesh was used. A higher mesh resolution was required for the case $\mu = 0.5$ than for $\mu = 0.1$.

5.4.3 Iterating SOSIA

Our assessment of the numerical validity and quality of the SOSIA revealed that two issues require further attention: First, the sensitivity of the SOSIA to σ_{res}, and possible problems

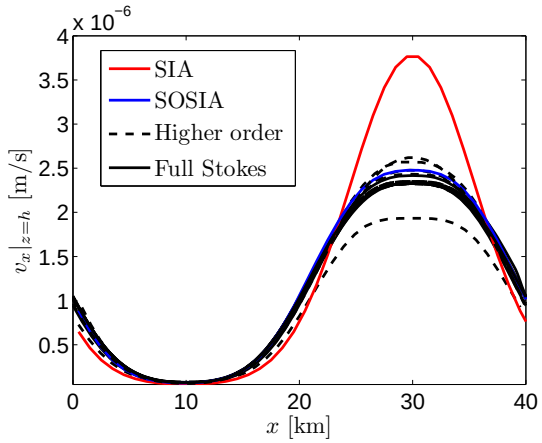

Fig. 9: Surface x-velocity for $L = 40$ km for the SIA and the SOSIA, together with full Stokes models and higher order models participating in the ISMIP-HOM benchmark B (**22**, **23**). The angle $\alpha = 0.5$ rad., $\sigma_{res} = 0$ for SIA, and for SOSIA $\sigma_{res} = \sqrt{10^9}$ and is added everywhere.

caused by it. Second, the absence of a strikingly obvious improvement when going from SIA to SOSIA. Indeed, with SOSIA only slightly better results are achieved where SIA already gives fairly good result, while SOSIA gets much worse than SIA when ϵ becomes too large. However, by solving SOSIA iteratively by repeatedly updating the solution in a loop, the sensitivity to σ_{res} decreases drastically, and the SOSIA solution is very close to the full Stokes solution even for large aspect ratios. Fig. 9 shows the SIA, the iterated SOSIA, the full Stokes solution and other higher order models for $L = 40$ km in the ISMIP-HOM benchmark B. For SOSIA, an optimal σ_{res} is *not* used, but simply chosen to be $\sqrt{10^9}$, as in Baral et al. (**6**). In the boundary layer, the normal deviatoric stresses need to be included to avoid singularities, and thus a Newton iteration is used to obtain them from Glen's flow law. For the shear stresses the SOSIA relations (28) are applied, where the zeroth order normal deviatoric stress is replaced by the normal deviatoric stress obtained from the Newton iteration. Once the vertical shear stress has been acquired, the velocities can be computed. A fixed-point iteration is applied to the whole system, improving the accuracy of the velocities in each step. If a more restrictive stopping criterion had been used, it is likely that SOSIA would have been even closer to the full Stokes solutions. The iterative scheme is attractive since it uses the information from the scaling assumptions in citeBlaHaftet,procrocsoc, which to hold fairly well outside the boundary layer, but the boundary layer has a negative effect on the convergence rate.

6. Discussion and Conclusions

We have numerically examined the validity of the scaling assumptions, which are the basis for shallow ice approximations. We have also solved the SIA and the SOSIA equations both analytically and numerically, and determined the accuracy compared to the full Stokes

equations. This was done for a model problem representing ice flow on a bumpy, sloping bed with no-slip conditions at the base, slightly modified from the ISMIP-HOM B benchmark set-up, (**22**). Extending the ISMIP HOM B set-up, we have not only varied the aspect ratio, ϵ, but also he inclination angle of the bed, α, and the amplitude of the bumps at the bed, μ. We now have the means to answer the questions posed in the introduction of this paper.

First, *How do the velocities, stresses and pressure vary with ϵ, and how do these scaling relations agree with the assumptions in Baral et al. (***7***, ***8***), Blatter (***9***) and Schoof & Hindmarsh (***11***)? Is there a boundary layer close to the ice surface where the field variables scale differently? Do scaling relations depend on other geometrical quantities than the aspect ratio ϵ, and if yes, on which and how?* By analysis in Sections 3 and 5.2, and numerical experiments in Section 4, we found that the assumptions about how the field variables vary with ϵ made in Baral et al. (**6**, **8**), Blatter (**9**) and Schoof & Hindmarsh (**11**) do not hold if the inclination angle, α, is independent of ϵ. An exception is the pressure, which agree quite well with both (**6**, **8**) and (**11**). We found that the angle should ideally be $\arctan(\epsilon)$ rad., agreeing with the common knowledge that slopes should be small for the scaling assumptions behind the shallow ice approximations to hold. Apparently, the angle should not only be small, but also vary with ϵ. Since many higher order models are based on scalings such as those in (**6**, **8**, **9**, **11**), it would have facilitated the analysis and comparison of the results in the ISMIP-HOM benchmark experiments (**22**) if it was designed such that $\alpha = \arctan(\epsilon)$ rad. instead of $\alpha = 0.5$ rad..

Letting the angle be $\arctan(\epsilon)$ rad. and $\mu \neq 0$ the numerical scaling relations, when considering the whole domain, agree with Baral et al. (**6**, **8**) for all field variables except for the normal deviatoric stress t^D_{xx}. Also, our numerical results and analytical solutions agree well with the velocity scalings in Blatter (**9**) and Schoof & Hindmarsh (**11**), i.e. the x-velocity is assumed to behave as $\mathcal{A}[H](\rho g[H])^3\epsilon^3$ and the z-velocity as $\mathcal{A}[H](\rho g[H])^3\epsilon^4$. By numerical experiments and analytical solutions in Section 4, we found that if the bed is flat, i.e. $\mu = 0$, the normal deviatoric stress t^D_{xx} varies with ϵ as assumed in (**6**, **8**), i.e. as ϵ^2. As soon as a small bump is introduced however, the character of the solution changes and t^D_{xx} varies as $\epsilon^{1.5}$ instead. The reason is that a boundary layer, where the viscosity is high, develops close to the ice surface due to the non-linear rheology whenever there are bumps at the ice base. Unless ϵ is extremely small, the boundary layer, as we define it, is very thick and there is no distinct border between the boundary layer (the inner region) and the region excluding the boundary layer (the outer region). We found that the boundary layer varies as $2.7[H]\epsilon^{0.26}$ for $\mu = 0.5$ and $2.2[H]\epsilon^{0.31}$ for $\mu = 0.1$, which compares fairly well to the theory in Johnson & McMeeking (**12**), and Schoof & Hindmarsh (**11**) who predicted the boundary layer to behave as $\mathcal{O}(\epsilon^{\frac{1}{3}})$. In Schoof & Hindmarsh (**11**) the stresses and the pressure are rescaled in this boundary layer such that all stress components are of equal importance, and this rescaling agrees very well with our numerical results for $\mu \neq 0$. One exception is the normal deviatoric stress, where the boundary layer effect spreads to the outer region, so that it behaves as $\epsilon^{1.6}$ or $\epsilon^{1.7}$ instead of the assumed ϵ^2 there. It would be interesting, but probably very complicated, to incorporate the importance of bumps at the bed in the theory by Schoof & Hindmarsh (**11**) such that it holds even for $\mu = 0$, allowing for a smooth transition to the theory in Baral et al. (**6**, **8**).

Our numerical scaling results agrees more with Baral et al. (**6**, **8**) and Schoof &

Hindmarsh (**11**) than with Blatter (**9**), and yet the Blatter-Pattyn equations which were originally derived from the scalings relations in (**9**) have proven very successful (**9**, **10**). This was rigorously explained by Schoof & Hindmarsh (**11**), but our results offer another viewpoint on this; in terms of the (uniform) scaling relations we obtain, the Blatter-Pattyn equations correspond to only discarding terms of $\mathcal{O}(\epsilon^2)$ or higher, and keeping those of $\mathcal{O}(\epsilon^{1.5})$ or lower.

Since the scaling relations of Baral et al. (**6**, **8**) do not account for the boundary layer and are only fully appropriate when there are no bumps at the bed or for the Newtonian ice, the next two questions in the introduction need to be answered; *Is the SIA and the SOSIA as accurate as the theory in Baral et al. (**6**) asserts? How should the non-linear, singular rheology of ice be treated in the SOSIA?* The SIA can be derived from several different scalings, and the fact that the scaling relations in (**6**, **8**) are not entirely correct for a bumpy bed does not mean that the SIA is an incorrect model. However, we find in our numerical experiments in Section 5.4 that the accuracy is not the expected $\mathcal{O}(\epsilon^2)$ for our model problem. The SOSIA is more sensitive to whether the scaling assumptions are correct than the SIA, and we find that, for a bumpy bed, SOSIA is not more accurate than SIA for all $\epsilon \leqslant 1$, as was expected from the perturbation expansion approach. For large (but still < 1), and very small ϵ, the SOSIA is *less* accurate than SIA.

Also, in SOSIA a parameter, σ_{res}, must be added to the creep response function in order to regularise the non-linear, singular rheology, since this is not accounted for in the scaling. From both analytical solutions to SOSIA and our numerical experiments, we find that the accuracy of the SOSIA velocity is very sensitive to how σ_{res} is used and what values of σ_{res} that are chosen, the vertical shear stress is less so. From our analytical solutions in Section 5.2 we infer that the relation $\sigma_{res} = C_\sigma \rho g[H]\epsilon$ should hold, and from our numerical results in Section 5.4 we find that σ_{res} should *not* be added everywhere, as suggested in Baral et al. (**6**), but rather be used as a lower threshold on the effective stress. For our model problem C_σ should be about 0.35, which means that the magnitude of σ_{res} should be about one third of the magnitude of the effective stress.

The accuracy of both SOSIA improves when the bump amplitude decreases, because the influence of σ_{res} is lower. For a bump amplitude of 50 % of the mean ice thickness, we can find a σ_{res} making the SOSIA more accurate than SIA for ϵ up to about 10^{-2}, while for a bump amplitude of 10 % of the mean thickness, SOSIA is more accurate than SIA for ϵ almost as large as 10^{-1}. Also for the SIA the accuracy is slightly higher for low bump amplitudes. This agrees with the common opinion that the bump amplitude should be low in order for shallow ice approximations to be valid.

Finally, only the last question remains to be answered; *Is the SOSIA a possible tool to tackle paleoglacial simulations?* Due to the sensitivity of SOSIA to σ_{res}, and since there are cases when SOSIA is less accurate than the SIA, we do not think it is appropriate to use SOSIA without automatic error control or iterations. This might on the other hand be fruitful, since information of the order of magnitude of the field variables are utilised without having to apply matched asymptotic expansions, and since we have shown that SOSIA loses its inconvenient sensitivity to the treatment of infinite viscosities when iterated. By improving the convergence rate of these iterations, the SOSIA may provide a useful model.

7. Acknowledgements

We are grateful to Kolumban Hutter for valuable discussions and comments during a stay in Uppsala, financed by the division of scientific computing at Uppsala University, and the Bert Bolin Center for Climate Research at Stockholm University.

References

1. H. Blatter, R. Greve, and A. Abe-Ouchi. Present State and Prospects of Ice Sheet and Glacier Modelling. *Surv. Geophys.*, **32**, (2011) 555–583.

2. N. Kirchner, K. Hutter, M. Jakobsson, and R. Gyllencreutz. Capabilities and limitations of numerical ice sheet models: a discussion for Earth-scientists and modelers. *Quaternary Sci. Rev.*, **30**, (2011), 3691–3704.

3. C. J. van der Veen, and ISMASS members. *A Need For More Realistic Ice-Sheet Models*, Report 30, International Council for Science, Scientific Committee on Antarctic Research (SCAR), Scott Polar Research Institute, Cambridge, United Kingdom, (2007).

4. K. Hutter. *Theoretical Glaciology.* D. Reidel, Dordrecht, (1983).

5. L. W. Morland. Thermo–mechanical balances of ice sheet flows. *Geophys. Astrophys. Fluid Dynam.*, **29**, (1984), 237–266.

6. D. R. Baral, K. Hutter, and R. Greve. Asymptotic theories of large-scale motion, temperature and moisture distribution in land-based polythermal ice sheets: A critical review and new developments. *Appl. Mech. Rev.*, **54**, (2001), 215–256.

7. D. R. Baral. *Asymptotic theories of large scale motion, temperature and moisture distributions in land based polythermal ice shields and in floating ice shelves. A critical reveiw and new developments.* PhD thesis, Department of Mechanics (III), Technical University Darmstadt, Germany, (1999).

8. R. Greve. A continuum-mechanical formulation for shallow polythermal ice sheets. *Phil. Trans. R. Soc. Lond.*. **A355**, 921–974, (1997).

9. H. Blatter. Velocity and stress fields in grounded glaciers: a simple algorithm for including deviatoric stress gradients. *J. Glaciol.*, **41**, (1995), 333–344.

10. F. Pattyn. A new three-dimensional higher-order thermomechanical ice sheet model: Basic sensitivity, ice stream development, and ice flow across subglacial lakes. *J. Geophys. Res.*, **108**, 2382, doi:10.1029/2002JB002329, (2003).

11. C. Schoof and R. C. A. Hindmarsh. Thin-Film Flows with Wall Slip: An Asymptotic Analysis of Higher Order Glacier Flow Models. *Quart, J. of Mech. Appl. Math.*, **63**, (2010), 73–114.

12. R. E. Johnson and R. M. McMeeking. Near-surface flow in glaciers obeying Glen's law. *Quart, J. of Mech. Appl. Math.*, **7**, (1984), 273–291.

13. L. A. Lliboutry. The dynamics of temperate glaciers from the detailed viewpoint. *J. Glaciol.*, **8**, (1969) 185–205.

14. S. C. Colbeck and R. J. Evans. A flow law for temperate glacier ice. *J. Glaciol.*, **12**, (1973), 71–86.

15. R. Calov, I. Marsiat. Simulations of the Northern Hemisphere through the last glacial-interglacial cycle with a vertically integrated and a three-dimensional thermomechanical ice-sheet model coupled to a climate model. *Ann. Glaciol.*, **27**, 169–176, (1998).

16. S. Charbit, C. Ritz, G. Philippon, V. Peyaud, M. Kageyama. Numerical reconstructions

of the Northern Hemisphere ice sheets through the last glacial-interglacial cycle. *Clim. Past*, **3**, 15–37, (2007).

17. P. L. Forsström, R. Greve. Simulation of the Eurasian ice sheet dynamics during the last glaciation. *Global Planet. Change*, **42**, 59–81, (2004).

18. R. Greve, M. Weis, K. Hutter. Paleoclimatic evolution and present conditions of the Greenland Ice Sheet in the vicinity of Summit: An approach by large-scale modeling. *Paleoclimates*, **2**, 133–161, (1998).

19. R. Greve, K. H. Wrywoll, A. Eisenhauer. Deglaciation of the Northern Hemisphere at the onset of the Eemian and Holocene. *Ann. Glaciol.*, **28**, 1–8, (1999).

20. E. le Meur, P. Huybrechts, A comparison of different ways of dealing with isostasy: examples from modeling the Antarctic ice sheet during the last glacial cycle. *Ann. Glaciol.*, **23**, 309–317, (1996).

21. I. Marsiat. Simulation of the Northern Hemsiphere continental ice sheets over the last glacial–intergalcial cycle: experiments with a latitude–longitude vertically integrated ice sheet model coupled to a zonally averaged climate model. *Paleoclimates*, **1**, 59–98, (1994).

22. F. Pattyn, L. Perichon, A. Aschwanden, B. Breuer, B. de Smedt, O. Gagliardini, G. H. Gudmundsson, R. Hindmarsh, A. Hubbard, J. V. Johnson, T. Kleiner, Y. Konovalov, C. Martin, A. J. Payne, D. Pollard, S. Price, M. Rückamp, F. Saito, O. Souček, S. Sugiyama, and T. Zwinger. Benchmark experiments for higher-order and full-Stokes ice sheet models (ISMIP-HOM). *The Cryosphere*, **2**, (2008), 95–108.

23. Website for the Ice Sheet Model Intercomparison Project for Higher-Order ice sheet Models (ISMIP-HOM). Available at: http://homepages.ulb.ac.be/fpattyn/ismip/, January 2011.

24. Elmer website, Available at: http://www.csc.fi/english/pages/elmer, March 2012.

25. E. le Meur, O. Gagliardini, T. Zwinger, and J. Ruokolainen. Glacier flow modelling: a comparison of the Shallow Ice Approximation and the full-Stokes solution. *C. R. Phys.*, **5**, (2004), 709–722.

26. R. C. A. Hindmarsh. A numerical comparison of approximations to the Stokes equations used in ice sheet and glacier modeling. *J. Geophys. Res.*, **109**, F01012, doi:10.1029/2003JF000065, (2004).

27. M. Schäfer. *Modélisation de l'écoulement des glaciers tempérés*. PhD thesis, Laboratoire de Glaciologie et Géophysique de l'Environment, Université Joseph Fourier, Grenoble, France, (2007).

28. A. Mangeney and F. Califano. The shallow-ice approximation for anisotropic ice - Formulation and limits. *J. Geophys. Res.*, **103**, 691–705, (1998).

29. D. L. Egholm, M. F. Knudsen, C. D. Clark, and J. E. Lesemann. Modeling the flow of glaciers in steep terrains: The integrated second-order shallow ice approximation (iSOSIA). *J. Geophys. Res.*, **116**, F02012, doi:10.1029/2010JF001900, (2011).

30. SICOPOLIS website, Available at: `sicopolis.greveweb.net`, June 2012.

31. R. Greve. *Thermomechanisches Verhalten polythermer Eisschilde - Theorie, Analytik, Numerik*. PhD thesis, Department of Mechanics (III), Technical University Darmstadt, Germany, (1995).

32. Elmer manual, Available at: http://www.nic.funet.fi/pub/sci/physics/elmer /doc/ElmerModelsManual.pdf, March 2012.

APPENDIX A

Analytical Solutions to the SIA and SOSIA

This appendix contain analytical solutions for $v_{x(0)}$, $v_{z(0)}$, $t^D_{xx(0)}$, $t^D_{xz(2)}$, $p_{(2)}$ and $v_{x(2)}$ for an isothermal, diagnostic, 2D-problem with no slip conditions at the base, an inclined plane as ice surface, and a zeroth order ice base. A finitie viscosity law on the form $f = \sigma^2 + \sigma^2_{res}$ is used, as discussed in Section 2.2.3. on the form For the model problem in Section 3 we also express the solutions in terms of L, α, μ, and σ_{res}.

A.1 *Zeroth Order x-velocity,* $v_{x(0)}$

Computing the integral in the second equation in (25) gives

$$v_{x(0)} = -2\rho g A(T') \frac{\partial h_{(0)}}{\partial x} \left(\frac{\left(\rho g \frac{\partial h_{(0)}}{\partial x}\right)^2}{4} \left(H^4 - (h_{(0)} - z)^4\right) + \frac{\sigma^2_{res}}{2} \left(H^2 - (h_{(0)} - z)^2\right) \right). \quad \text{(A.1)}$$

Inserting the expressions for h, b and H (see equation (12)) yields (31).

A.2 *Zeroth Order z-velocity,* $v_{z(0)}$

The z-velocity $v_{z(0)}$ is given by

$$\begin{aligned} v_{z(0)} &= \int_{b_{(0)}}^{z} \frac{\partial v_{x(0)}}{\partial x} dz' \qquad \text{(A.2)} \\ &= 2A(T') \frac{\partial h_{(0)}}{\partial x} \left((\rho g)^3 \left(\frac{\partial h_{(0)}}{\partial x} \right)^2 \left(H^3_{(0)} \frac{\partial H_{(0)}}{\partial x} (z - b_{(0)}) + \frac{1}{4} \frac{\partial h_{(0)}}{\partial x} \left((h_{(0)} - z)^4 - H^4_{(0)} \right) \right) \right. \\ &+ \left. \rho g \sigma^2_{res} \left(H_{(0)} \frac{\partial H_{(0)}}{\partial x} (z - b_{(0)}) + \frac{1}{2} \frac{\partial h_{(0)}}{\partial x} \left((h_{(0)} - z)^2 - H^2_{(0)} \right) \right) \right). \end{aligned}$$

Inserting the expressions for h, b and H (see equation (12)) yields

$$\begin{aligned} v_{z(0)} &= 2\mathcal{A}(\rho g)^3 \tan^3(\alpha) \Big([H]^4 \left(1 - \mu \sin(2\pi x/L)\right)^3 \mu \frac{2\pi}{L} \cos(2\pi x/L) \qquad \text{(A.3)} \\ &\cdot \left(z + x \tan(\alpha) + [H] \left(1 - \mu \sin(2\pi x/L)\right)\right) \\ &+ \frac{1}{4} \tan(\alpha) (x \tan(\alpha) + z)^4 - [H]^4 \left(1 - \mu \sin(2\pi x/L)\right)^4 \Big) + 2\mathcal{A}\rho g \sigma^2_{res} \tan(\alpha) \\ &\cdot \Big([H]^2 \left(1 - \mu \sin(2\pi x/L)\right) \mu \frac{2\pi}{L} \cos(2\pi x/L) \left(z + x \tan(\alpha) + [H] \left(1 - \mu \sin(2\pi x/L)\right)\right) \Big). \end{aligned}$$

A.3 *Zeroth Order Normal Deviatoric Stress,* $t^D_{xx(0)}$

Inserting equation (45) in (26) gives

$$\begin{aligned} t^D_{xx(0)} &= \frac{-2\rho g \frac{\partial h_{(0)}}{\partial x}}{\left(\left(\left(h_{(0)} - z\right) \frac{\partial h_{(0)}}{\partial x} \right)^2 + \left(\frac{\sigma_{res}}{\rho g} \right)^2 \right)} \left(\left(\frac{\partial h_{(0)}}{\partial x} \right)^2 \left(H^3 \frac{\partial H_{(0)}}{\partial x} - \frac{\partial h_{(0)}}{\partial x} (h_{(0)} - z)^3 \right) \right. \\ &+ \left. \left(\frac{\sigma_{res}}{\rho g} \right)^2 \left(H \frac{\partial H_{(0)}}{\partial x} - \frac{\partial h_{(0)}}{\partial x} (h_{(0)} - z) \right) \right). \qquad \text{(A.4)} \end{aligned}$$

Inserting the expressions for h, b and H (equation (12)) yields (32).

A.4 *Second Order Vertical Shear Stress,* $t^D_{xz(2)}$

Inserting equation (48) in (28) knowing that $t^D_{zz} = -t^D_{xx}$ gives

$$\begin{aligned}\epsilon^2 t^D_{xz(2)} &= 3\rho g\left(\frac{\partial h_{(0)}}{\partial x}\right)^3 (h_{(0)}-z) - \frac{4(\rho g)^2}{\sigma_{res}}\left(3H^2\left(\frac{\partial H_{(0)}}{\partial x}\right)^2\left(\frac{\partial h_{(0)}}{\partial x}\right)^2 + H^3\frac{\partial^2 H}{\partial x^2}\left(\frac{\partial h_{(0)}}{\partial x}\right)^2\right.\\ &+ \left.\frac{\sigma^2_{res}}{(\rho g)^2}\left(\left(\frac{\partial H_{(0)}}{\partial x}\right)^2 + H_{(0)}\frac{\partial^2 H_{(0)}}{\partial x^2}\right)\right)\arctan\left(\rho g\frac{\frac{\partial h_{(0)}}{\partial x}(h_{(0)}-z)}{\sigma_{res}}\right)\\ &- 4\rho g\frac{H_{(0)}\frac{\partial H_{(0)}}{\partial x}\left(\frac{\partial h_{(0)}}{\partial x}\right)^2\left(\left(\frac{\partial h_{(0)}}{\partial x}\right)^2 H^2_{(0)} + \frac{\sigma^2_{res}}{(\rho g)^2}\right)}{\left(\frac{\partial h_{(0)}}{\partial x}\right)^2(h_{(0)}-z)^2 + \frac{\sigma^2_{res}}{(\rho g)^2}}.\end{aligned} \tag{A.5}$$

Inserting the expressions for h, b and H (equation (12)) yields (33).

A.5 *Second Order Pressure,* $p_{(2)}$

The calculation of the second order pressure from equation (27) is straight forward, knowing that $t^D_{zz} = -t^D_{xx}$ and using equation (48) and equation (32).

A.6 *Second Order x-velocity,* $v_{x(2)}$

Inserting the expressions for $t^D_{xz(0)}$,$t^D_{xx(0)}$, and $t^D_{xz(2)}$ in (29) gives

$$\begin{aligned}\frac{\epsilon^2 v_{x(2)}}{A(T')} &= -\left(z-b_{(0)}\right)^2\left(\left(\rho g\frac{\partial h_{(0)}}{\partial x}\right)^3\left(3H^2_{(0)}\left(\frac{\partial H_{(0)}}{\partial x}\right)^2 + H^3_{(0)}\frac{\partial^2 H_{(0)}}{\partial x^2}\right)\right.\\ &+ \left.\rho g\frac{\partial h_{(0)}}{\partial x}\sigma^2_{res}\left(\left(\frac{\partial H_{(0)}}{\partial x}\right)^2 + H_{(0)}\frac{\partial^2 H_{(0)}}{\partial x^2}\right)\right) +\\ &- 4\left(h_{(0)}-z\right)^2\frac{\partial h_{(0)}}{\partial x}(\rho g)^3\left(3H^2\left(\frac{\partial H_{(0)}}{\partial x}\right)^2\left(\frac{\partial h_{(0)}}{\partial x}\right)^2 + H^3\frac{\partial^2 H}{\partial x^2}\left(\frac{\partial h_{(0)}}{\partial x}\right)^2\right.\\ &+ \left.\frac{\sigma^2_{res}}{(\rho g)^2}\left(\left(\frac{\partial H_{(0)}}{\partial x}\right)^2 + H_{(0)}\frac{\partial^2 H_{(0)}}{\partial x^2}\right)\right) + 4\left(h_{(0)}-z\right)^2\sigma^2_{res}\rho g\left(\frac{\partial h_{(0)}}{\partial x}\right)^3\\ &+ \left(b_{(0)}-z\right)\left(6\left(\rho g\right)^3\left(\frac{\partial h_{(0)}}{\partial x}\right)^4 H^3_{(0)}\frac{\partial H_{(0)}}{\partial x} + 6\rho g\sigma^2_{res}\left(\frac{\partial h_{(0)}}{\partial x}\right)^2 H_{(0)}\frac{\partial H_{(0)}}{\partial x}\right.\\ &- \left.2\left(\rho g\frac{\partial h_{(0)}}{\partial x}\right)^3 H^3_{(0)}\frac{\partial H_{(0)}}{\partial x}\frac{\partial b_{(0)}}{\partial x}\right) -\\ &+ 8\left(\frac{\partial h_{(0)}}{\partial x}\right)^2\frac{(\rho g)^4}{\sigma_{res}}\left(3H^2\left(\frac{\partial H_{(0)}}{\partial x}\right)^2\left(\frac{\partial h_{(0)}}{\partial x}\right)^2 + H^3\frac{\partial^2 H}{\partial x^2}\left(\frac{\partial h_{(0)}}{\partial x}\right)^2 +\right.\\ &+ \left.\frac{\sigma^2_{res}}{(\rho g)^2}\left(\left(\frac{\partial H_{(0)}}{\partial x}\right)^2 + H_{(0)}\frac{\partial^2 H_{(0)}}{\partial x^2}\right)\right)(h_{(0)}-z)^3\arctan\left(\frac{\frac{\partial h_{(0)}}{\partial x}\rho g}{\sigma_{res}}(h_{(0)}-z)\right)\\ &- 4\left(\rho g\right)^3\frac{\partial h_{(0)}}{\partial x}\frac{\left(\left(\frac{\partial h_{(0)}}{\partial x}\right)^2 H^3\frac{\partial H_{(0)}}{\partial x} + \frac{\sigma^2_{res}}{(\rho g)^2}H\frac{\partial H_{(0)}}{\partial x}\right)^2}{\left(\frac{\partial h_{(0)}}{\partial x}\right)^2(h_{(0)}-z)^2 + \frac{\sigma^2_{res}}{(\rho g)^2}} - 2\left(\frac{\partial h_{(0)}}{\partial x}\right)^5(\rho g)^3(h_{(0)}-z)^4\end{aligned} \tag{A.6}$$

$$
\begin{aligned}
&+ \quad 8\sigma_{res}(\rho g)^2\left(3H^2\left(\frac{\partial H_{(0)}}{\partial x}\right)^2\left(\frac{\partial h_{(0)}}{\partial x}\right)^2 + H^3\frac{\partial^2 H}{\partial x^2}\left(\frac{\partial h_{(0)}}{\partial x}\right)^2\right.\\
&+ \quad \left.\frac{\sigma_{res}^2}{(\rho g)^2}\left(\left(\frac{\partial H_{(0)}}{\partial x}\right)^2 + H_{(0)}\frac{\partial^2 H_{(0)}}{\partial x^2}\right)\right)(h_{(0)}-z)\arctan\left(\frac{\frac{\partial h_{(0)}}{\partial x}\rho g}{\sigma_{res}}(h_{(0)}-z)\right)\\
&+ \quad 2\rho g\frac{\partial h_{(0)}}{\partial x}\sigma_{res}^2 H_{(0)}\frac{\partial H_{(0)}}{\partial x}\frac{\partial b_{(0)}}{\partial x}(z-b_{(0)})\\
&- \quad \frac{8(\rho g)^2}{\sigma_{res}}\left(\left(\frac{\partial h_{(0)}}{\partial x}\right)^2(\rho g)^2 H_{(0)}^2 + \sigma_{res}^2\right)\left(3H^2\left(\frac{\partial H_{(0)}}{\partial x}\right)^2\left(\frac{\partial h_{(0)}}{\partial x}\right)^2 + H^3\frac{\partial^2 H}{\partial x^2}\left(\frac{\partial h_{(0)}}{\partial x}\right)^2\right.\\
&+ \quad \left.\frac{\sigma_{res}^2}{(\rho g)^2}\left(\left(\frac{\partial H_{(0)}}{\partial x}\right)^2 + H_{(0)}\frac{\partial^2 H_{(0)}}{\partial x^2}\right)\right)H_{(0)}\arctan\left(\frac{\frac{\partial h_{(0)}}{\partial x}\rho g}{\sigma_{res}}H_{(0)}\right) + 2\left(\frac{\partial h_{(0)}}{\partial x}\right)^5(\rho g)^3 H_{(0)}^4\\
&+ \quad 16\,(\rho g)^3\,H_{(0)}^4\left(\frac{\partial H_{(0)}}{\partial x}\right)^2\left(\frac{\partial h_{(0)}}{\partial x}\right)^3 + 8\rho g\frac{\partial h_{(0)}}{\partial x}H_{(0)}^2\left(\frac{\partial H_{(0)}}{\partial x}\right)^2\sigma_{res}^2\\
&- \quad 4\sigma_{res}^2\rho g\left(\frac{\partial h_{(0)}}{\partial x}\right)^3 H_{(0)}^2 + 4(\rho g)^3 H_{(0)}^5\frac{\partial^2 H}{\partial x^2}\left(\frac{\partial h_{(0)}}{\partial x}\right)^3 + 4\frac{\partial h_{(0)}}{\partial x}\rho g H_{(0)}^3\sigma_{res}^2\frac{\partial^2 H_{(0)}}{\partial x^2}.
\end{aligned}
$$

Inserting the expressions for h, b and H (equation (12)) yields

$$
\begin{aligned}
&\frac{\epsilon^2 v_{x(2)}}{A(T')} = \left(\frac{2\pi}{L}\right)^2\mu[H]^3\left(z + x\tan(\alpha) - (\mu\sin(2\pi x/L)-1)\right)^2 \qquad (A.7)\\
&\cdot \quad \left((\rho g\tan(\alpha))^3[H]^2\Big(3\mu\left(1-\mu\sin(2\pi x/L)\right)^2\cos^2(2\pi x/L) + \left(1-\mu\sin(2\pi x/L)\right)^3\sin(2\pi x/L)\Big)\right.\\
&+ \quad \left.\rho g{\sigma_{res}}^2\tan(\alpha)\Big(\mu\cos^2(2\pi x/L) + (1-\mu\sin(2\pi x/L))\sin(2\pi x/L)\Big)\right)\\
&+ \quad 4(\rho g)^3[H]^4\left(\frac{2\pi}{L}\right)^2\mu\tan(\alpha)\left(x\tan(\alpha)+z\right)^2\left(3\left(1-\mu\sin(2\pi x/L)\right)^2\mu\cos^2(2\pi x/L)\tan^2(\alpha)\right.\\
&+ \quad \left(1-\mu\sin(2\pi x/L)\right)^3\sin(2\pi x/L)\tan^2(\alpha)\\
&+ \quad \left.\frac{{\sigma_{res}}^2}{(\rho g)^2}\Big(\mu\cos^2(2\pi x/L) + (1-\mu\sin(2\pi x/L))\sin(2\pi x/L)\Big)\right)\\
&- \quad 4\sigma_{res}^2\rho g\tan^3(\alpha)\mu\frac{2\pi}{L}\left(x\tan(\alpha)+z\right)^2\Big(x\tan(\alpha) - [H]\left(\mu\sin(2\pi x/L)-1\right) + z\Big)\cos(2\pi x/L)\\
&\cdot \quad \left(6[H]^4\left(\rho g\right)^3\tan^4(\alpha)\left(1-\mu\sin(2\pi x/L)\right)^3 - 6[H]^2\rho g{\sigma_{res}}^2\tan^2(\alpha)\left(1-\mu\sin(2\pi x/L)\right) + \right.\\
&- \quad \left.2[H]^4\left(\rho g\tan(\alpha)\right)^3\left(1-\mu\sin(2\pi x/L)\right)^3\left(-\tan(\alpha) + [H]\frac{2\pi}{L}\mu\cos(2\pi x/L)\right)\right)\\
&- \quad 8(\rho g)^4\frac{[H]^4}{\sigma_{res}}\left(\frac{2\pi}{L}\right)^2\mu\tan^2(\alpha)\left(3\left(1-\mu\sin(2\pi x/L)\right)^2\mu\cos^2(2\pi x/L)\tan^2(\alpha)\right.\\
&+ \quad \left.\left(1-\mu\sin(2\pi x/L)\right)^3\sin(2\pi x/L)\tan^2(\alpha)\right.
\end{aligned}
$$

$$
\begin{aligned}
&+ \quad \frac{{\sigma_{res}}^2}{(\rho g)^2}\Big(\mu\cos^2(2\pi x/L) + (1-\mu\sin(2\pi x/L))\sin(2\pi x/L)\Big)\Bigg) \\
&\cdot \quad (x\tan(\alpha)+z)^3 \arctan\left(\frac{\tan(\alpha)\rho g}{\sigma_{res}}(x\tan(\alpha)+z)\right) \\
&+ \quad 4\,(\rho g)^3\tan(\alpha)\left(\frac{2\pi}{L}\right)^2\mu^2[H]^4 \\
&\cdot \quad \frac{\cos^2(2\pi x/L)\,(1-\mu\sin(2\pi x/L))^2\left(\tan^2(\alpha)[H]^2\,(1-\mu\sin(2\pi x/L))^2+\frac{{\sigma_{res}}^2}{(\rho g)^2}\right)^2}{\tan^2(\alpha)(x\tan(\alpha)+z)^2+\frac{{\sigma_{res}}^2}{(\rho g)^2}} \\
&+ \quad 2(\rho g)^3\,(\tan(\alpha))^5\,(x\tan(\alpha)+z)^4 \\
&- \quad 8\sigma_{res}(\rho g)^2[H]^4\left(\frac{2\pi}{L}\right)^2\mu\Bigg(3\,(1-\mu\sin(2\pi x/L))^2\,\mu\cos^2(2\pi x/L)\tan^2(\alpha) \\
&+ \quad (1-\mu\sin(2\pi x/L))^3\sin(2\pi x/L)\tan^2(\alpha) \\
&+ \quad \frac{{\sigma_{res}}^2}{(\rho g)^2}\Big(\mu\cos^2(2\pi x/L) + (1-\mu\sin(2\pi x/L))\sin(2\pi x/L)\Big)\Bigg)(x\tan(\alpha)+z) \\
&\cdot \quad \arctan\left(\frac{\tan(\alpha)\rho g}{\sigma_{res}}(x\tan(\alpha)+z)\right) \\
&+ \quad 2\frac{2\pi}{L}\mu\rho g{\sigma_{res}}^2[H]^2\tan(\alpha)\,(1-\mu\sin(2\pi x/L))\cos(2\pi x/L)\left(-\tan(\alpha)+[H]\frac{2\pi}{L}\mu\cos(2\pi x/L)\right) \\
&\cdot \quad (z+x\tan(\alpha)-[H](\mu\sin(2\pi x/L)-1)) \\
&- \quad 8(\rho g)^2\frac{[H]^5}{\sigma_{res}}\left(\frac{2\pi}{L}\right)^2\mu\Bigg(3\,(1-\mu\sin(2\pi x/L))^2\,\mu\cos^2(2\pi x/L)\tan^2(\alpha) \\
&+ \quad (1-\mu\sin(2\pi x/L))^3\sin(2\pi x/L)\tan^2(\alpha) \\
&+ \quad \frac{{\sigma_{res}}^2}{(\rho g)^2}\Big(\mu\cos^2(2\pi x/L) + (1-\mu\sin(2\pi x/L))\sin(2\pi x/L)\Big)\Bigg)\,(1-\mu\sin(2\pi x/L)) \\
&\cdot \quad \left(\tan^2(\alpha)(\rho g)^2[H]^2\,(1-\mu\sin(2\pi x/L))^2+{\sigma_{res}}^2\right)\arctan\left(\frac{-\tan(\alpha)\rho g}{\sigma_{res}}[H]\,(1-\mu\sin(2\pi x/L))\right) \\
&- \quad 2[H]^4\,(\tan(\alpha))^5\,(\rho g)^3\,(1-\mu\sin(2\pi x/L))^4 \\
&- \quad 16\,(\rho g)^3\,[H]^6\left(\frac{2\pi}{L}\right)^2\mu^2\,(1-\mu\sin(2\pi x/L))^4\,(\cos(2\pi x/L))^2\,(\tan(\alpha))^3 \\
&- \quad 8[H]^4\rho g{\sigma_{res}}^2\left(\frac{2\pi}{L}\right)^2\mu^2\tan(\alpha)\,(1-\mu\sin(2\pi x/L))^2\,(\cos(2\pi x/L))^2 \\
&+ \quad 4{\sigma_{res}}^2\rho g[H]^2\,(\tan(\alpha))^3\,(1-\mu\sin(2\pi x/L))^2 \\
&- \quad 4[H]^6(\rho g)^3\left(\frac{2\pi}{L}\right)^2\mu\,(1-\mu\sin(2\pi x/L))^5\sin(2\pi x/L)\,(\tan(\alpha))^3 \\
&- \quad 4[H]^4{\sigma_{res}}^2\left(\frac{2\pi}{L}\right)^2\mu\tan(\alpha)\rho g\,(1-\mu\sin(2\pi x/L))^3\sin(2\pi x/L).
\end{aligned}
$$